

Multi-Object Spectroscopy of Galaxy Clusters at $z \sim 0.95$ in Ultra Deep Survey Field with Different Star-formation Properties and Large-scale Environments

SEONG-KOOK LEE,^{1,2} MYUNGSHIN IM,^{1,2} BOMI PARK,^{1,2} MINHEE HYUN,³ INSU PAEK,^{1,2} AND DOHYEONG KIM⁴

¹*SNU Astronomy Research Center, Department of Physics and Astronomy, Seoul National University, Seoul, Korea*

²*Astronomy Program, Department of Physics and Astronomy, Seoul National University, Seoul, Korea*

³*Korea Astronomy and Space Science Institute, Daejeon, Korea*

⁴*Department of Earth Sciences, Pusan National University, Busan, Korea*

ABSTRACT

While galaxy clusters are dominated by quiescent galaxies at local, they show a wide range in quiescent galaxy fraction (QF) at higher redshifts. Here, we present the discovery of two galaxy clusters at $z \sim 0.95$ with contrasting QFs despite having similar masses ($\log (M_{200}/M_{\odot}) \sim 14$) and spectra and redshifts of 29 galaxies in these clusters and 76 galaxies in the surrounding area. The clusters are found in the Ultra Deep Survey (UDS) field and confirmed through multi-object spectroscopic (MOS) observation using the Inamori Magellan Areal Camera and Spectrograph (IMACS) on the Magellan telescope. The two clusters exhibit QFs of $0.094^{+0.11}_{-0.032}$ and $0.38^{+0.14}_{-0.11}$, respectively. Analysis of large-scale structures (LSSs) surrounding these clusters finds that properties of these clusters are consistent with the anti-correlation trend between the QF and the extent of surrounding LSS, found in Lee et al. (2019), which can be interpreted as a result from the replenishment of young, star-forming galaxies keeps the QF low when galaxy clusters are accompanied by rich surrounding environments.

Keywords: Galaxy clusters (584) — High-redshift galaxy clusters(2007) — Galaxy evolution(594) — High-redshift galaxies(734) — Large-scale structure of the universe(902) — Cosmic web(330)

1. INTRODUCTION

Understanding the evolution of star formation properties of galaxies has profound implications for the study of galaxy evolution and cosmology. A galaxy's star formation history (SFH) is intricately tied to its overall evolution, with different galaxy types exhibiting distinct patterns in their SFHs (e.g. Longhetti et al. 1999; Clemens et al. 2006; Fitzpatrick & Graves 2015). Tracing the evolution of star formation properties provides valuable insights into the processes governing the transformation and evolution of galaxies from one type to another (Kennicutt 1998; Heavens et al. 2004; Renzini 2009). Also, the star formation rate (SFR) in galaxies has varied across cosmic time. Examining this variation allows us to deduce the cosmic star formation history (SFH) of the universe, unveiling when the peak of star formation occurred and how it has evolved over time (Madau et al. 1996; Hartwick 2004; Heavens et al. 2004; Madau & Dickinson 2014). The evolution of star formation properties also offers valuable constraints for cosmological models. For instance, it can aid in testing predictions related to dark matter, dark energy, and the large-scale structure (LSS) of the universe. Comparing observed SFRs with theoretical predictions from models proves beneficial in refining our comprehension of cosmological models (e.g. Henriques et al. 2015; Knebe et al. 2015; Somerville & Davé 2015; Vogelsberger et al. 2020).

Corresponding author: Seong-Kook Lee
s.joshualee@gmail.com

Corresponding author: Myungshin Im
myungshin.im@gmail.com

In this regards, it is particularly crucial to investigate how star formation in galaxies evolves or ceases. Understanding the processes governing star formation evolution unravels the lifecycles of galaxies. Galaxies undergo various development stages, transitioning from active star-forming phases to quiescent states. Studying these transitions provides insights into the factors driving galaxies to change over cosmic time.

Star formation is a intricate process that entails interactions among gas, dust, and stars. Feedback mechanisms, such as stellar winds and supernovae, play a crucial role in regulating star formation by expelling gas and heating the interstellar medium. Consequently, understanding both the cessation of star formation and the intricate connection between star formation and feedback processes is essential for gaining insights into how galaxies autonomously regulate their growth and how these processes influence various galaxy properties.

The proposed quenching mechanisms can generally categorized into two types: internal and external. The internal mechanisms are reflected in the correlation between the star formation rate (SFR) and stellar mass (Kauffmann et al. 2003; Jimenez et al. 2005; Baldry et al. 2006), while external mechanisms are manifested in the correlation between the SFR and the environment (Lewis et al. 2002; Kauffmann et al. 2004; Baldry et al. 2006). Numerous studies have delved into the relative importance and effects of these internal and external quenching processes (e.g., Peng et al. 2010; Lee et al. 2015; Chartab et al. 2020; Gu et al. 2021).

In the present-day universe, many galaxies in dense environments exhibit little to no ongoing star formation activity, leading to a distinct environment-dependent bimodality. However, observational evidence indicates that this environment-dependent bimodality weakens at higher redshifts. By redshift $z \sim 1$, this environmental dependence of galaxy properties becomes notably weak (Scoville et al. 2013). Additionally, the gap in quiescent galaxy fraction (QF) between clusters and the field also diminishes with increasing redshift (e.g., Lee et al. 2015; Papovich et al. 2018; Lemaux et al. 2019; Sarron & Conselice 2021). This suggests that galaxies in clusters are actively forming stars, similar to their counterparts in the field at this redshift, in contrast to the local universe.

To understand the diminishing environmental dependence with increasing redshift, it is essential to explore the evolution of star formation properties within the context of galaxy cluster formation and evolution. Galaxies that fall into a cluster undergo various physical quenching mechanisms, such as ram pressure stripping (Gunn & Gott 1972; Abadi et al. 1999), strangulation (Larson et al. 1980; Balogh et al. 2000; Peng et al. 2015) and galaxy harassment (Moore et al. 1996), operating on different timescales. It is plausible that galaxies recently entering clusters at high redshift ($z > 1.5$) may not have had sufficient time to undergo quenching.

Moreover, alongside the reduced environmental dependence on star formation activity in galaxies at $z \sim 1$, individual galaxy clusters exhibit significant variation in their star formation status, such as QF (Lee et al. 2015; Alberts et al. 2016; Hayashi et al. 2019; Lee et al. 2019). However, it remains unclear what factors contribute to the observed cluster-by-cluster variation in the star formation properties of high-redshift ($z > 0.5$) galaxy clusters.

At high redshift, many galaxy clusters are still growing by accreting gas and galaxies from their surrounding environment. These accreted materials may contribute to maintaining a large fraction of star-forming galaxies within the clusters (Ellingson et al. 2001; Tran et al. 2005; Lubin et al. 2009; Lee et al. 2019). In our recent study (Lee et al. 2019) conducted in the Ultra Deep Survey (UDS; Almaini et al. 2007) field, we demonstrated a correlation between the QF of a galaxy cluster and the extent of the large-scale structures connected to the cluster. This suggests that the large-scale environment surrounding galaxy clusters, acting as a reservoir of gas and star-forming galaxies, can influence the star-formation status of clusters. In Lee et al. (2019), we proposed the web-feeding model (WFM) to explain this phenomenon.

The aforementioned discoveries underscore the necessity for a thorough investigation into the star formation properties and the surrounding environment of high-redshift galaxy clusters. The research presented in this paper reflects our continuous efforts to understand the star formation status of galaxy clusters and their associated large-scale structures.

In this study, we present two newly spectroscopically confirmed galaxy clusters at $z \sim 0.95$ in the UDS field and provide redshifts for 105 galaxies within these clusters and the surrounding area. Our aim is to investigate the star formation properties and characteristics of the surrounding large-scale structures associated with these clusters. This redshift range has been recognized as a critical period for the environmental quenching of star formation activity in galaxies (e.g., Peng et al. 2010; Sobral et al. 2011; Quadri et al. 2012; Lee et al. 2015; Lu et al. 2021; McNab et al. 2021).

In Section 2, we offer a detailed explanation of the data, including cluster sample, spectroscopic observations, data reduction procedure, and redshift measurements. Utilizing the spectroscopic data and redshift measurements, we confirm the clusters and explore the properties of both the clusters themselves and their member galaxies in Section

3. Section 4 is dedicated to presenting the correlation between the QF and the extent of the connected large-scale structure surrounding these clusters. Additionally, we discuss the QFs of these clusters, considering their dependence on stellar mass.

We adopt a standard cosmology with $(\Omega_m, \Omega_\Lambda) = (0.3, 0.7)$ and $H_0 = 70 \text{ km s}^{-1} \text{ Mpc}^{-1}$, consistent with observations over the past decades (e.g. Im et al. 1997). All magnitudes are given in the AB magnitude system (Oke 1974).

2. DATA AND SAMPLE

2.1. Photometric Data

2.1.1. Multiwavelength Data

The UDS field carries a wealth of multi-band photometric data collected from various facilities across approximately 0.8 deg^2 . In this study, we utilize optical data from the Subaru telescope, near-infrared (NIR) data from the United Kingdom InfraRed Telescope (UKIRT), and mid-infrared (MIR) data from the Infrared Array Camera (IRAC) on the Spitzer telescope for conducting photometric redshift calculation and estimating stellar population properties through spectral energy distribution (SED) fitting.

The optical broad-band photometric data are obtained from the SUPRIMECAM on the Subaru telescope (SXDS; Furusawa et al. 2008), with $3\text{-}\sigma$ magnitude limits at each band as $B = 28.4, V = 27.8, R = 27.7, i' = 27.7$, and $z' = 26.7$. NIR photometric data are from the WFCAM on the UKIRT (UKIDSS; Lawrence et al. 2007), with $5\text{-}\sigma$ magnitude limits of $J = 25.2, H = 24.7$, and $K_s = 24.9$. The MIR data are from the Spitzer/IRAC as the SpUDS Spitzer Legacy Survey (PI: Dunlop), with depths of $\sim 24 \text{ mag}$ in channels 1 and 2. For the Subaru/SUPRIMECAM and UKIRT/WFCAM data, auto magnitudes are used, while aperture-corrected total magnitudes are used for the Spitzer/IRAC data. For further information on the photometry and the reliability of using the auto magnitudes, refer to Lee et al. (2015).

In addition to these data sets, we use MIR data from the Multiband Imaging Photometer for Spitzer (MIPS) to explore dusty star-forming galaxies. As mentioned above, the UDS region was covered by the SpUDS survey, which includes MIR data from Spitzer/IRAC as well as MIPS $24 \mu\text{m}$. The depth of MIPS $24 \mu\text{m}$ is $\sim 80 \nu\text{Jy}$, which corresponds to $\text{SFR} \sim 20 \text{ M}_\odot/\text{yr}$ at $z \sim 1$ (Caputi et al. 2006). In this study, we investigate the MIPS image data and catalog within the Magellan-observed region to identify any MIPS sources (i.e. dusty SF galaxies) within and around the cluster region.

2.1.2. Photometric Redshift Estimation and SED Fitting

Utilizing the aforementioned multiwavelength data, we estimate the photometric redshifts and stellar population properties, such as stellar mass, and SFR, for the galaxies in our sample, as explained in Lee et al. (2015) in detail. In brief, we utilized optical, NIR, and MIR broadband data to estimate the photometric redshifts using EAZY (Brammer et al. 2008). We employ the K -band magnitude prior, as it yields slightly improved accuracy in photometric redshifts.

To derive the stellar population properties of galaxies, we used our own SED-fitting code (Lee et al. 2009) assuming delayed star-formation histories (SFHs) (Lee et al. 2010), with a functional form to describe the star formation rate at a given time t as

$$\Psi(t, \tau) \propto \frac{t}{\tau^2} e^{-t/\tau}, \quad (1)$$

where t represents the time since the onset of star formation and τ is the timescale parameter that governs the rate at which the SFR reaches its peak value.

The delayed SFH has been shown to well represent the actual SFHs of high-redshift galaxies (e.g. Pacifici et al. 2013; Lee et al. 2014).

For the SED-fitting, we employ ~ 4000 spectral templates derived from the updated version of the BC03 model (Bruzual & Charlot 2003), assuming the Chabrier (2003) initial mass function (IMF). We incorporate internal dust attenuation using the Calzetti law (Calzetti et al. 2000), while the intergalactic medium (IGM) dust attenuation follows the Madau law (Madau 1995). After estimating the stellar population properties, we apply a stellar mass cut ($\log(M_*/M_\odot) \geq 9.1$) to our sample.

Through the SED-fitting process, various parameters are derived for each galaxy, including stellar mass (M_*), age (t), star formation timescale (τ), metallicity (Z), and color excess ($E(B-V)$). For more detailed information regarding photometric redshift estimation and our SED-fitting process for our sample galaxies, please refer to Lee et al. (2015).

2.2. Spectroscopy

2.2.1. Target Selection

In Lee et al. (2015), we identified galaxy cluster candidates within the redshift range of $0.5 \leq z \leq 2.0$ in the UDS field. These cluster candidates were identified based on photometric redshifts, identifying structures with galaxy number densities exceeding the 4σ level. Please refer Lee et al. (2015) for more details about our cluster candidate selection method. The reliability of our cluster selection method has been well demonstrated in our previous work (Lee et al. 2019) and also in Sarron & Conselice (2021).

From the galaxy cluster candidate list in Lee et al. (2015), we selected several cluster candidates for follow-up spectroscopic observations, among which the observation and analysis of two $z \sim 0.95$ cluster candidates is presented in this paper. These two cluster candidates were chosen due to their distinct star formation properties, despite being at similar redshifts and separated by only ~ 4 Mpc.

Subsequently, we identified galaxies within and surrounding these selected cluster candidates for spectroscopic follow-up observations. The selection of target galaxies was based on their photometric redshifts, R -band magnitudes, and proximity to the candidate clusters. During the design of masks for the multi-object spectroscopic (MOS) observation, priority values were assigned to galaxies based on these specific galaxy properties. Galaxies with brighter R -band magnitudes and closer proximity to the candidate clusters were given higher priority.

2.2.2. Magellan Observation

We conducted observations of two galaxy cluster candidates and their surrounding regions using the Inamori-Magellan Areal Camera and Spectrograph (IMACS) on the Magellan/Baade telescope. These two candidate clusters are at similar redshifts of $z \sim 0.95$ and are separated by ~ 4 Mpc.

employing the Magellan/IMACS $f/2$ camera, we performed multiobject spectroscopic (MOS) observations on twice occasions – firstly on August 27, 2016 (2016B semester) and subsequently on August 31, 2019 (2019B semester). 179 out of total 538 slits were assigned within $9' \times 18'$ sky region ($34.0^\circ - 34.15^\circ$ in R.A., and $-5.0^\circ - -4.7^\circ$ in declination), covering the cluster candidates and their surrounding regions. The other 359 slits were allocated in the remaining mask area, targeting different cluster candidates and LSSs at different photometric redshifts. The spectroscopic data obtained from these remaining slits will be presented in our future work. For each mask, we assigned a slit for a standard (K -type) star for flux calibration.

The slit length and width were $6 \text{ arcsec} \times 1 \text{ arcsec}$. The exposure times for each run were 2 hours for the 2016B run and 1.5 hours for the 2019B run. In both runs, the exposure time was divided into four and three 30-min exposures, respectively. The average seeing were 1.5 arcsec for the 2016B run and 1 arcsec for the 2019B run. We utilized a Grism with 200 lines per millimetre and the WB6300-9500 filter for the 2016B run, and the WBP5694-9819 filter for the 2019B run, providing wavelength coverage of 630~950 nm (570~980 nm) with a spectral resolution of $R \sim 650$. These settings ensured adequate coverage of major spectroscopic features of the galaxies under investigation.

2.2.3. Data Reduction

Data reduction was performed using the latest version of the Carnegie Observatories System for Multi-Object Spectroscopy software (COSMOS2), which is the software package provided by Carnegie Observatories for reduction of spectroscopic data obtained with the IMACS instrument. We followed the same reduction procedure as outlined in Lee et al. (2019). For wavelength calibration, He-Ne-Ar arc frames were used. Following the standard COSMOS2 routine, flat fielding and bias subtraction were conducted on the science frames. After sky subtraction, two-dimensional (2D) spectra were extracted and combined into a single 2D spectrum, The bulk of cosmic rays were removed in this process. For further details, please consult the COSMOS cookbook (Oemler et al. 2017). One-dimensional (1D) spectra were subsequently extracted from the combined 2D spectrum, employing an extraction width corresponding to twice the average seeing values. Flux calibration was done using a standard star — the same star for both masks — included in each mask. Flux-calibrated spectra are available as machine-readable tables, with an example presented in Appendix A (Table A1).

2.2.4. Redshift Measurement

From the extracted 1D spectra, galaxy redshifts were determined using the SpecPro software (Masters & Capak 2011). Key spectral features utilized for redshift identification of galaxies within the redshift range of $0.8 < z < 1.1$ are [O II] $\lambda 3727$, $H\beta$, $H\gamma$, and [O III] emission lines, along with Ca H&K and G -band absorption lines.

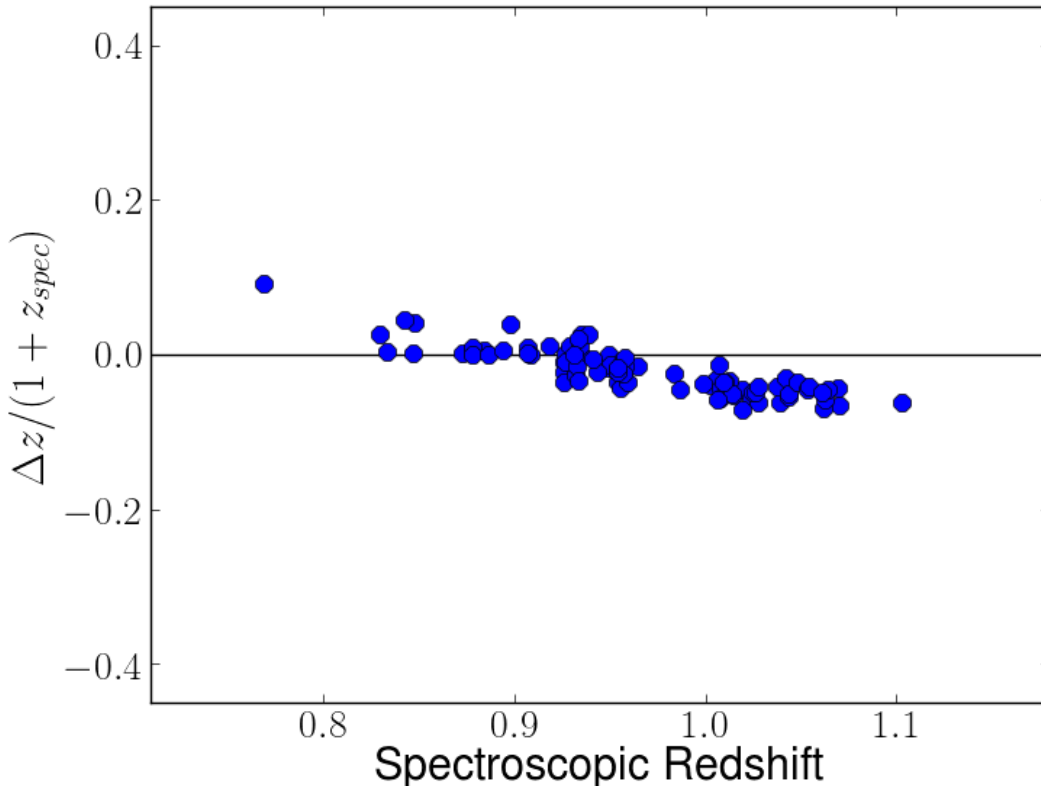


Figure 1. Photometric redshift error ($\Delta z/(1+z)$) as a function of spectroscopic redshift. Photometric redshift errors are small in the range of $0.8 < z < 1.0$.

For many galaxies at the redshift of cluster candidates ($z \sim 0.95$), redshift measurements rely on a single emission line feature, [O II] $\lambda 3727$. Despite this reliance on a single emission line, our redshift determination is reliable for the following reasons: (1) the absence of other prominent emission lines that would be expected if the identified line were not [O II] (such as H β or [O III]), indicating a lower redshift, and (2) a close correspondence between the photometric redshift obtained from multi-band SEDs and the measured redshift, within the uncertainty of the photometric redshift.

We assign the quality flag ‘a’ to galaxies with secure redshift measurements based on clear emission line(s) or absorption feature(s). For galaxies where emission or absorption line(s) are faint, we assign the quality flag ‘b’. Out of 177 galaxies for which slits were assigned, redshifts could be measured for 105 galaxies. Among these, 76 were assigned the flag ‘a’, and 29 were assigned the flag ‘b’. Therefore, the redshift measurement rate is 66% (44% for galaxies with the flag ‘a’ only). The normalized median absolute deviation (NMAD) of $\Delta z/(1+z)$ for galaxies with flag ‘a’ galaxies is 0.024, and NMAD for galaxies with flag ‘a’ or ‘b’ is 0.030. For subsequent analysis, only spectroscopic redshifts with the ‘a’ flag are utilized.

Figure 1 shows the photometric redshift error as a function of spectroscopic redshift for spectroscopically confirmed 105 galaxies. This figure shows that the photometric redshifts are very accurate in the redshift range of $0.8 < z < 1.0$.

The top panel of Figure 2 shows the Subaru R -band magnitude distribution of our 177 spectroscopic target galaxies (grey histogram) alongside the distribution of 76 galaxies whose spectroscopic redshifts were measured with the ‘a’ flag (black histogram). Given that the R -band magnitude was used in determining the priority of spectroscopic targets, the number of target galaxies rapidly decrease at $R > 24$ mag. While faint galaxies down to $R \sim 27$ mag are included in our target, reliable spectroscopic redshift measurements can only be obtained down to $R \sim 24.5$ mag.

The bottom panel of Figure 2 presents the R -band magnitude-dependent redshift measurement rate. The black symbols and line depict the redshift measurement rate of all galaxies with spectroscopic redshifts measured with the flag ‘a’. As can be seen in this figure, the redshift measurement rate declines with increasing R magnitude, although it remains at $\sim 50\%$ down to $R \sim 23.5$. The green and red lines represent the redshift measurement rates of blue

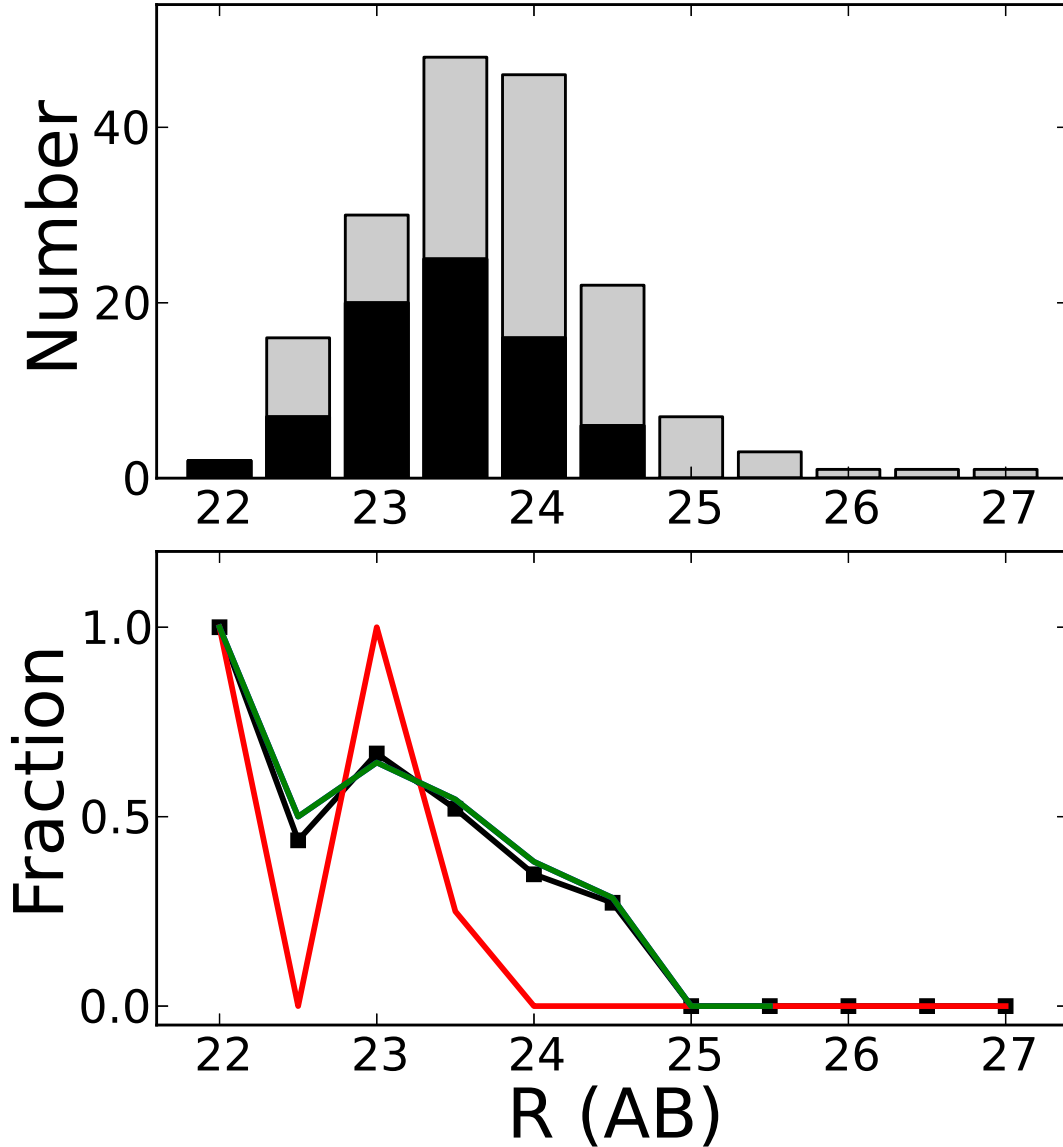


Figure 2. (Top) Distributions of R magnitude of our target galaxies (grey histogram) and of galaxies whose spectroscopic redshifts are measured with flag ‘a’ (black histogram). (Bottom) R magnitude-dependent redshift measurement rate for blue ($R - z' < 1.5$; green line), red ($R - z' > 1.5$; red line) and total (black symbols and black line) galaxies with flag ‘a’.

($R - z' < 1.5$) and red ($R - z' > 1.5$) galaxies, respectively. Although faint red galaxies are included in our target selection, the measurement rate sharply declines at $R > 23$ due to the requirement of spectroscopic confirmation involving the detection and measurement of continuum and absorption spectral features.

We provide a complete list of galaxies with measured spectroscopic redshifts in Table 1, and present several example spectra of galaxies in Figure 3.

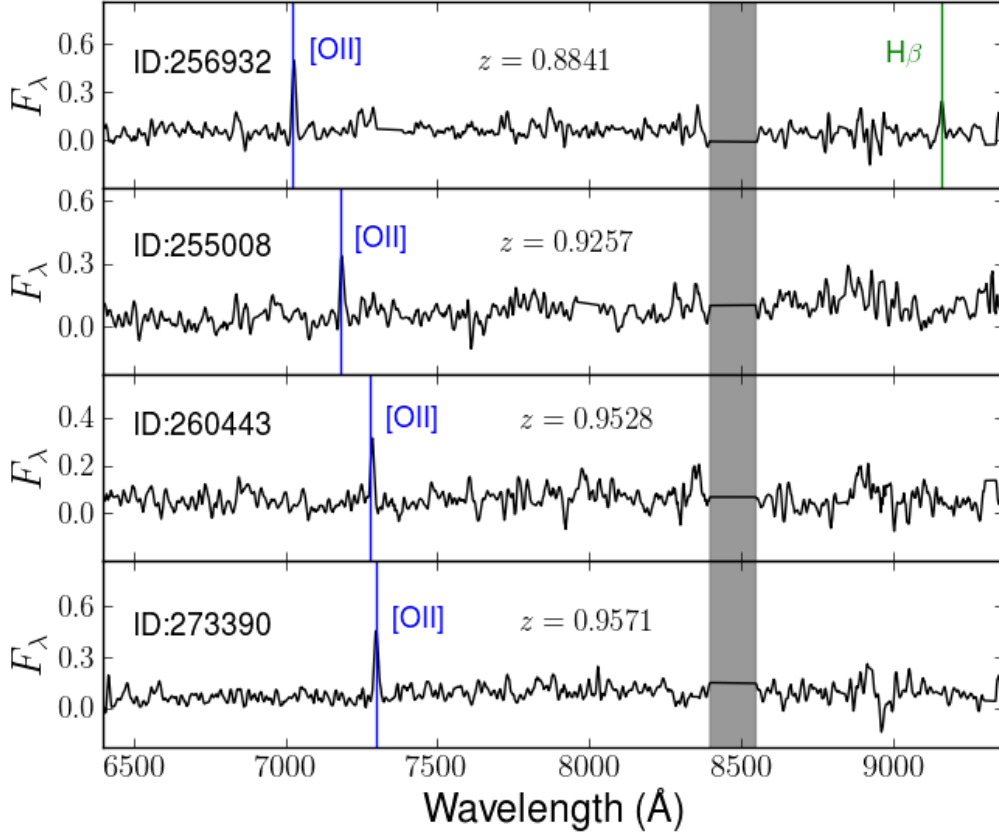


Figure 3. Example spectra of galaxies with redshift measurements obtained from our Magellan/IMACS observation. Among these galaxies, two are at $z \sim 0.95$ and are associated with UDS-OD5. The y -axis is in the unit of $10^{-17} \text{ erg s}^{-1} \text{ cm}^{-2} \text{ \AA}^{-1}$.

Table 1. Spectroscopic redshift information from Magellan/IMACS observation

ID	R.A. (J2000)	Dec. (J2000)	z_{spec}	flag	feature	z_{phot}	R_{AB}	Cluster ID
(1)	(2)	(3)	(4)	(5)	(6)	(7)	(8)	(9)
244417	34.05622	-4.99749	0.9522	b	1	0.987	23.239	–
245714	34.04414	-4.99579	0.8979	b	4	0.973	22.343	–
250613	34.08777	-4.98057	0.9432	b	1	0.900	22.865	–
251538	34.08322	-4.97781	1.0196	b	1	0.877	22.847	–
252172	34.05969	-4.97543	1.0700	a	1	0.936	22.621	–
255008	34.04831	-4.96708	0.9257	a	1	0.907	22.779	–
256349	34.04827	-4.96348	1.0389	a	1	0.913	22.859	–
256932	34.05170	-4.96175	0.8841	a	1, 2	0.895	23.411	–
257855	34.06900	-4.95946	1.0026	b	3	0.925	24.687	–
258156	34.06051	-4.95882	0.9269	a	1	0.930	23.721	–
260443	34.05391	-4.95191	0.9528	a	1	0.932	23.477	OD5
264268	34.09649	-4.94119	1.0481	b	1	0.975	23.503	–

Table 1 continued on next page

Table 1 (*continued*)

ID	R.A. (J2000)	Dec. (J2000)	z_{spec}	flag	feature	z_{phot}	R_{AB}	Cluster ID
(1)	(2)	(3)	(4)	(5)	(6)	(7)	(8)	(9)
265309	34.04951	-4.93914	0.9568	b	1	0.910	22.562	OD5
265593	34.03121	-4.93778	1.0374	a	1	0.952	22.870	–
267056	34.12305	-4.93415	1.0139	a	1	0.922	22.577	–
267126	34.12066	-4.93504	1.0142	b	1, 3	0.912	22.747	–
267460	34.12469	-4.93288	1.0149	a	1	0.908	23.876	–
270520	34.02529	-4.92377	1.0536	b	1	0.961	23.477	–
271494	34.01935	-4.92221	1.0542	b	1	0.968	23.819	–
271834	34.04345	-4.91991	0.9574	a	1	0.895	22.958	OD5
273315	34.10436	-4.91658	0.9288	a	4	0.949	23.160	–
273390	34.07657	-4.91531	0.9571	a	1	0.914	23.570	OD5
274769	34.06047	-4.91084	1.0129	a	1	0.925	23.900	–
275297	34.10982	-4.90982	0.9560	a	1	0.887	23.000	OD5
275833	34.06886	-4.90789	0.8733	a	1, 2	0.876	23.577	–
276591	34.11271	-4.90561	0.9542	a	1	0.906	24.317	OD5
277018	34.12688	-4.90440	1.0615	a	1	0.920	24.212	–
277503	34.04987	-4.90333	1.0612	b	1	0.959	24.173	–
278883	34.07732	-4.90045	1.0690	a	1	0.981	23.490	–
279334	34.03289	-4.89895	0.9539	a	1	0.885	22.620	OD5
279446	34.05863	-4.89776	1.0624	a	1	0.941	23.287	–
280515	34.04927	-4.89640	0.9556	a	1, 3	0.870	22.185	OD5
280801	34.05230	-4.89432	0.9343	b	3	0.957	22.301	–
281193	34.07362	-4.89516	1.0132	a	1, 3	0.916	22.428	–
282124	34.10719	-4.88912	0.9278	a	1	0.906	23.826	–
282407	34.05711	-4.89196	0.8864	b	3	0.886	22.546	–
283044	34.06182	-4.88738	0.9263	a	1	0.883	23.017	–
285119	34.01437	-4.88162	0.9389	b	3	0.989	22.849	–
285422	34.02600	-4.87971	0.9502	a	1	0.933	23.682	OD5
285957	34.10335	-4.87837	0.9585	b	3	0.925	24.143	OD5
286455	34.04077	-4.87675	0.9537	a	1	0.937	23.174	OD5
286983	34.01588	-4.87473	0.9497	a	1	0.931	23.522	OD5
287071	34.04088	-4.87489	0.9579	a	1, 3	0.949	24.02	OD5
287799	34.03378	-4.87290	0.9480	a	1, 3	0.914	23.686	OD5
288650	34.04529	-4.87064	0.9539	b	1	0.910	24.021	OD5
289803	34.07054	-4.86697	1.0437	a	1	0.933	23.603	–
291771	34.02039	-4.86163	0.9328	b	3	0.903	24.088	–
293978	34.04612	-4.85510	0.9496	a	1	0.951	23.795	OD5
294085	34.12790	-4.85608	1.0419	a	1	0.979	22.755	–
295199	34.08322	-4.85155	0.9563	a	1	0.911	24.076	OD5
296511	34.09816	-4.84826	1.0437	a	1	0.942	23.701	–
299918	34.05652	-4.84142	0.9555	a	1	0.936	23.490	OD5

Table 1 *continued on next page*

Table 1 (*continued*)

ID	R.A. (J2000)	Dec. (J2000)	z_{spec}	flag	feature	z_{phot}	R_{AB}	Cluster ID
(1)	(2)	(3)	(4)	(5)	(6)	(7)	(8)	(9)
300128	34.09291	-4.83823	0.9501	a	1	0.923	23.865	OD5
300247	34.05586	-4.83826	1.0057	a	1	0.941	23.494	–
302274	34.09396	-4.83384	0.9338	b	3	0.975	23.077	–
302482	34.04108	-4.83204	0.9541	a	1	0.912	23.080	OD5
302663	34.07093	-4.83091	1.0096	b	1	0.939	24.232	–
304508	34.02532	-4.82624	0.8477	a	1, 6	0.924	23.216	–
304910	34.09086	-4.82549	0.9561	a	1	0.919	22.514	OD5
306231	34.10122	-4.82172	0.8334	a	1, 2, 6, 7	0.840	23.174	–
306600	34.10518	-4.82173	1.1027	a	1	0.971	22.493	–
307616	34.13180	-4.81764	1.0196	a	1	0.928	23.339	–
307680	34.12864	-4.81722	0.9517	b	1	0.930	24.452	–
308869	34.01946	-4.81459	0.8786	a	3, 4	0.897	23.252	–
309350	34.01620	-4.81266	0.8940	b	1, 3	0.906	24.062	–
310759	34.07322	-4.80818	0.9987	a	1, 3	0.923	24.166	–
312083	34.13118	-4.80484	0.9069	b	1, 5	0.911	24.309	–
312773	34.03048	-4.80246	0.9650	a	1, 3	0.937	23.972	–
314583	34.12050	-4.79875	1.0126	a	1	0.945	22.992	–
314733	34.13864	-4.79779	0.9069	a	1, 2, 7	0.926	23.030	–
315279	34.02424	-4.79571	1.0278	b	1	0.945	24.163	–
316009	34.12718	-4.79397	0.9187	a	1	0.939	24.098	–
316036	34.13282	-4.79524	0.9087	a	1	0.910	22.994	–
317272	34.02931	-4.79094	1.0240	a	1	0.909	23.649	–
318139	34.04814	-4.78929	0.9258	a	1	0.858	23.853	OD6
318872	34.05303	-4.78640	1.0100	a	1	0.937	23.277	–
320222	34.13063	-4.78334	0.7690	b	3, 4	0.933	22.722	–
321245	34.09541	-4.77970	0.9539	b	3	0.922	23.737	–
321954	34.12612	-4.77666	0.8781	a	1	0.879	24.020	–
322784	34.08195	-4.77559	0.9303	a	1	0.912	24.245	OD6
323555	34.08519	-4.77300	0.9865	b	3	0.896	23.589	–
326976	34.09032	-4.76285	1.0077	a	1, 3	0.923	23.646	–
327269	34.11302	-4.76144	0.9563	a	1, 3	0.934	24.471	–
329647	34.02022	-4.75503	0.8471	a	1, 6	0.849	23.617	–
329905	34.09185	-4.75558	0.9339	b	1, 3	0.867	24.204	OD6
330837	34.13920	-4.75191	0.9560	a	1	0.912	23.437	–
333013	34.14636	-4.74600	1.0276	a	1, 3	0.903	24.321	–
333403	34.01790	-4.74555	0.9592	a	1	0.888	23.445	–
333438	34.07702	-4.74511	0.9835	a	1	0.935	23.087	–
334775	34.04690	-4.74118	1.0064	b	1	0.889	24.020	–
335066	34.10069	-4.74156	0.9308	a	3	0.918	23.103	OD6
336397	34.13436	-4.73659	1.0244	a	1	0.925	24.004	–

Table 1 *continued on next page*

Table 1 (*continued*)

ID	R.A. (J2000)	Dec. (J2000)	z_{spec}	flag	feature	z_{phot}	R_{AB}	Cluster ID
(1)	(2)	(3)	(4)	(5)	(6)	(7)	(8)	(9)
336469	34.04198	-4.73725	1.0071	a	1	0.982	23.184	–
337933	34.01030	-4.73300	1.0082	a	1	0.894	22.706	–
337967	34.02968	-4.73159	0.9578	a	1	0.927	23.930	–
338563	34.02084	-4.73197	0.9310	a	3, 4	0.901	22.228	OD6
339103	34.08369	-4.72883	0.9543	a	1, 3, 5	0.916	23.462	–
340617	34.07509	-4.72401	0.9271	a	1	0.909	24.386	OD6
343044	34.07878	-4.71893	0.8430	b	3, 4	0.926	23.281	–
343667	34.09394	-4.71544	1.0640	a	1	0.972	24.343	–
344164	34.03337	-4.71439	0.9320	a	3	0.883	23.674	OD6
345206	34.10844	-4.71122	1.0261	a	1	0.926	23.308	–
348499	34.07541	-4.70168	0.8301	a	1, 6	0.878	23.100	–
350746	34.06160	-4.69843	0.9355	a	3, 4	0.937	22.912	OD6
350989	34.05905	-4.69616	0.9411	b	3	0.930	23.312	–

NOTE—(1) Object ID; (2) R. A. (degree); (3) Declination (degree); (4) Spectroscopic redshift; (5) Spectroscopic flag; (6) Redshift identification feature – 1: [O II], 2: H β , 3: Ca H&K, 4: 4000 Å break, 5: H δ , 6: [O III], 7: H γ ; (7) Photometric redshift; (8) R -band magnitude (AB); (9) Associated cluster ID

2.2.5. Slit Loss Correction

For the spectra of galaxies in Table 1, we compared the synthetic i' -band photometry derived from the flux-calibrated Magellan spectra with the photometric measurements obtained from Subaru data. The differences between these two sets of magnitudes, as shown in Figure 4, indicate systematic offsets. These offsets result from the differences between the width of the spectrograph slit and the angular sizes of the observed galaxies. This phenomenon, known as slit loss, exhibits a correlation with the magnitude of galaxies, with brighter galaxies experiencing more significant slit loss.

We extended this comparison to the Rc -band photometry and found a similar magnitude-dependent trend as well as comparable slit loss values to those observed in the i' -band. The difference between the Rc and i' -band correction factors indicates the accuracy of flux calibration. We found that these two factors agree within 0.05 (Figure 5), suggesting flux calibration accuracy of 5%, which becomes to 3% for brighter magnitudes ($i' < 23$).

We provide the correction factors, which correspond to the reciprocal of the calculated slit loss values from the i' -band analysis, in a separate machine-readable table. A portion of this table is shown in Table 2.

3. RESULTS

3.1. Cluster Confirmation

From the spectroscopic redshift data described in Section 2.2.4, we confirm two galaxy clusters. The first cluster is located at R.A.= 34.0539 and Dec.= -4.87675 with a redshift of $z \sim 0.954$. The second cluster is located at R.A.= 34.0616 and Dec.= -4.73197 with $z \sim 0.931$. We refer to these confirmed clusters as UDS-OD5 and UDS-OD6, respectively.

Initially, among the galaxies with spectroscopic redshifts, we identify potential cluster members based on their rest-frame relative velocities, which should fall within ± 1500 km/s and within $3 \times R_{200}$ (see Section 3.2 for the derivation of R_{200}).

The final confirmation of cluster members is obtained by investigating the ‘distance–velocity’ phase diagram (see Figure 6). We have identified a total of 18 galaxies (with the flag ‘a’) as confirmed members of UDS-OD5, and 7 galaxies (with the flag ‘a’) as confirmed members of UDS-OD6. Additionally, there are 3 member galaxies with the

Table 2. The correction factors calculated in the i' -band for each galaxy.

ID	Correction Factor
244417	1.67
245714	3.21
250613	2.49
251538	2.41
252172	1.89
255008	3.11
256349	1.79
256932	1.49
257855	1.28
.....

NOTE—Table 2 is published in its entirety in the machine-readable format. A portion is shown here for guidance regarding its form and content.

flag ‘b’ in UDS-OD5 and 1 member galaxy with the flag ‘b’ in UDS-OD6. In the subsequent analysis, we will only consider the galaxies with the flag ‘a’.

In Figure 7, we show the distributions of spectroscopic redshifts (with the flag ‘a’) for galaxies located within $3 \times R_{200}$ from the cluster center. In this figure, the red histogram shows the galaxies confirmed as members of each cluster. In the redshift distribution of UDS-OD6 (right panel), we can identify a prominent peak at $z \sim 0.93$ which shows the galaxies belonging to UDS-OD6. Additionally, there is a secondary peak at $z \sim 0.95$, as well as two minor peaks at $z > 1$. The presence of the second peak at $z \sim 0.95$ in the redshift distribution can also be confirmed in the phase diagram in Figure 6. In the phase diagram of the right panel in this figure, several galaxies with a relative velocity of $\sim 4000 \text{ km s}^{-1}$ belong to the UDS-OD5, and some galaxies with similar relative velocities but smaller distances may belong to this second redshift peak. Although it is challenging to clearly identify due to the spatial overlap with UDS-OD6, some of these galaxies may be part of the filamentary structure connected to UDS-OD5.

3.2. Halo Properties of Confirmed Clusters

From the spectroscopic redshift information of the confirmed member galaxies, we can estimate the sizes and masses of the confirmed clusters as follows.

3.2.1. UDS-OD5

The center of the cluster is determined as the median location of the spectroscopically confirmed member galaxies. This center coincides with the peak of the galaxy number density distribution in this region.

For the estimation of the halo mass and size, we first calculate the velocity dispersion of the cluster from the distribution of spectroscopic redshifts of the confirmed members. We employ the gapper estimator (Beers et al. 1990) for this purpose. The calculated velocity dispersion is $\sigma_v = 553 \pm 87 \text{ km s}^{-1}$, where the error is determined using the *jackknife* method. From this σ_v , we estimate R_{200} and M_{200} following the method by Demarco et al. (2010), as follows:

$$R_{200} = \frac{\sqrt{3}\sigma_v}{10H(z)} \quad (2)$$

and

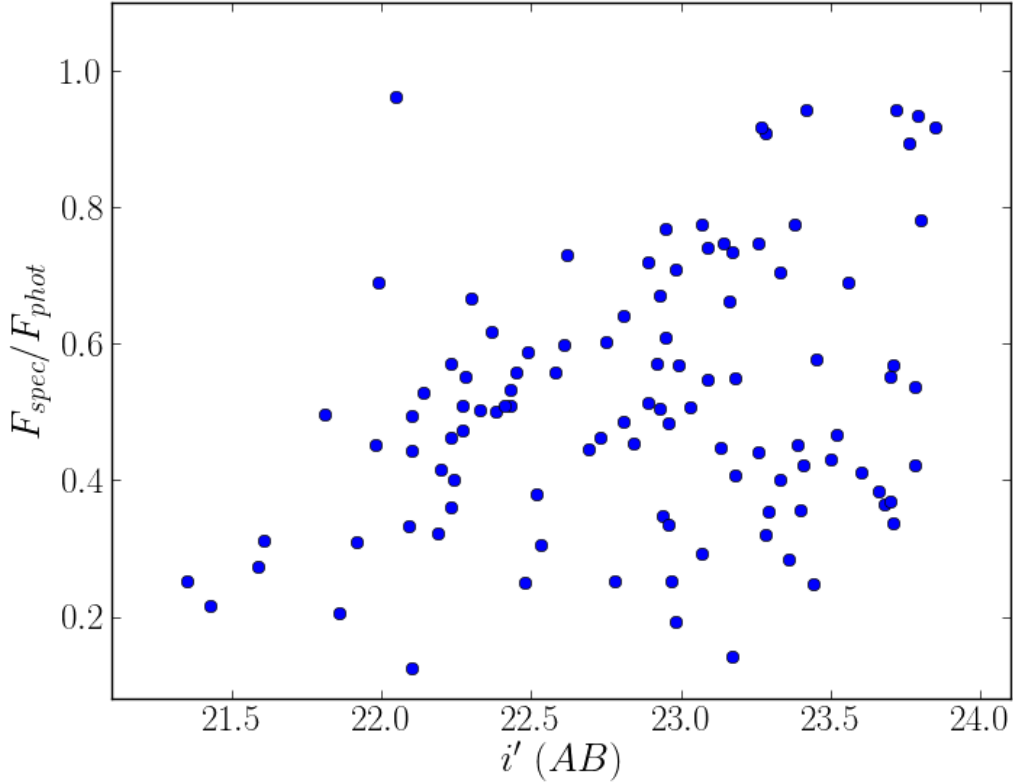


Figure 4. The fraction of fluxes derived from synthetic photometry based on the flux-calibrated spectra (F_{spec}) compared to the corresponding values obtained from Subaru data (F_{phot}) in i' -band as a function of i' magnitude. The disparities between these two flux values tend to be more significant for brighter galaxies.

$$M_{200} = 3 \frac{\sigma_v^2 R_{200}}{G}. \quad (3)$$

Here, $H(z)$ is the Hubble constant at redshift z . The radius and halo mass of UDS-OD5 are calculated as $R_{200} = 799 \pm 126$ kpc and $M_{200} = 1.70^{+0.94}_{-0.68} \times 10^{14} M_{\odot}$. We also estimate the halo mass from the total stellar mass of galaxies, following Lee et al. (2019), and applying the weight to cluster candidates as explained in Section 4.1. This method gives the halo mass to be $1.16^{+0.90}_{-0.51} \times 10^{14} M_{\odot}$, in agreement with the halo mass estimated from velocity dispersion.

3.2.2. UDS-OD6

The other cluster, UDS-OD6, is located north of UDS-OD5, and at a slightly lower redshift of $z \sim 0.931$.

The velocity dispersion, measured using the Gapper estimator, of the UDS-OD6 is $\sigma_v = 518 \pm 178$ km s $^{-1}$. The calculated radius and halo mass from the velocity dispersion are $R_{200} = 758 \pm 261$ kpc and $M_{200} = 1.42^{+2.03}_{-1.02} \times 10^{14} M_{\odot}$. The halo mass from total stellar mass is $1.27^{+0.99}_{-0.56} \times 10^{14} M_{\odot}$. From this, we can see that these two clusters, UDS-OD5 and UDS-OD6, have very similar mass and size.

3.3. Properties of Candidate Member Galaxies of Confirmed Clusters

3.3.1. Red Galaxies

Figure 8 shows the correlation between stellar mass and $R-z'$ color of galaxies whose redshifts are within the photometric redshift error range ($\Delta z/(1+z_{cl}) = 0.028$). The top panels of this figure show galaxies located within $3 \times R_{200}$ from the cluster center, and the bottom panels show galaxies within R_{200} . In this figure, red squares are red quiescent galaxies whose $R-z'$ color is redder than 1.5. This color cut is shown as a red horizontal line in each panel. There is a well-developed red sequence in the regions containing both clusters, especially for massive galaxies

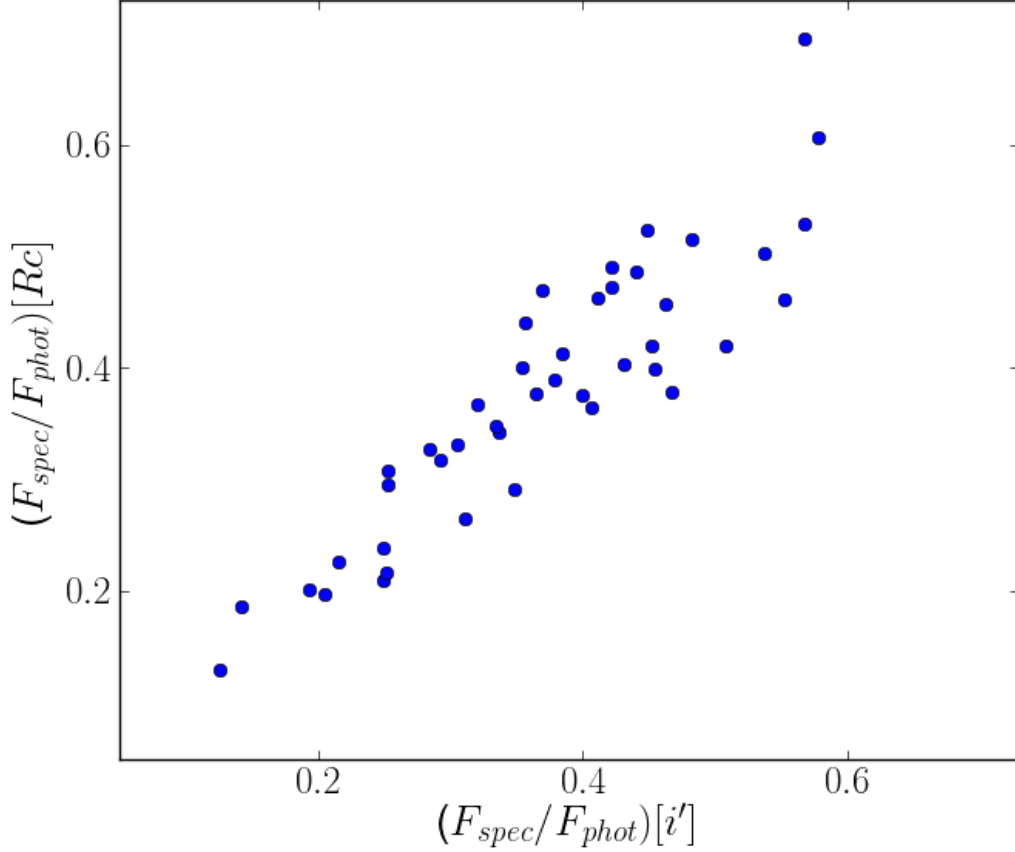


Figure 5. A comparison of the fraction of fluxes (F_{spec}/F_{phot}) obtained in Rc -band (x -axis) and i' -band (y -axis). These two values are similar, following a one-to-one relation.

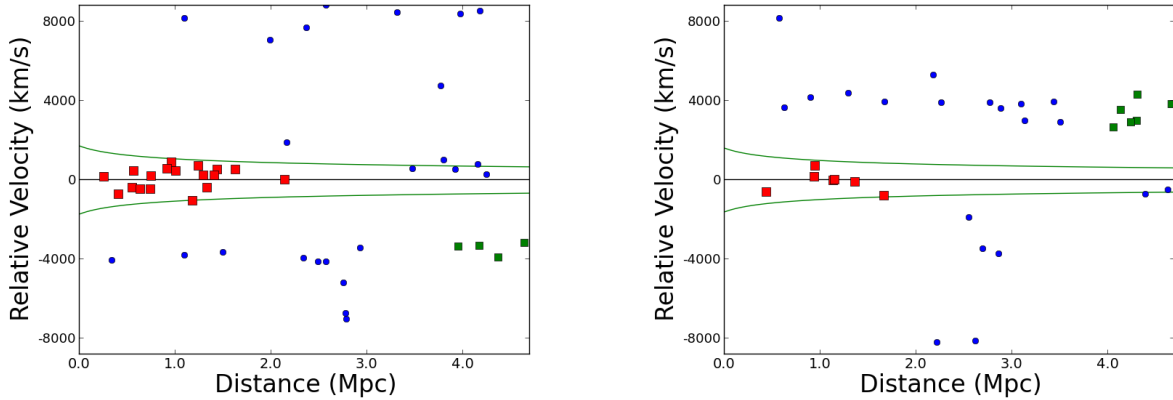


Figure 6. [Left] ‘Distance–relative velocity’ phase diagrams of UDS-OD5. Only galaxies with the spectroscopic flag ‘a’ are shown, and the spectroscopically confirmed cluster members are represented by red squares. Galaxies represented by green squares are the confirmed members of UDS-OD6. Galaxies represented by blue dots are not members of either cluster. [Right] ‘Distance–relative velocity’ phase diagrams of UDS-OD6, and details are same as the left figure. Some galaxies represented by blue dots at relative velocity of $\sim 4000 \text{ km s}^{-1}$ are the galaxies belonging to the large-scale structure connected to UDS-OD5.

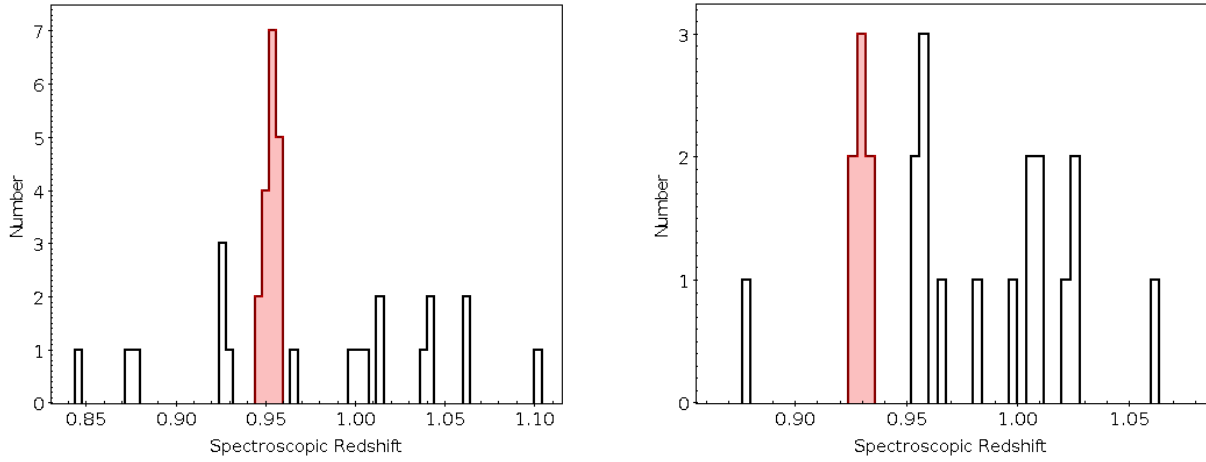


Figure 7. The distributions of spectroscopic redshifts (with the flag ‘a’) for galaxies within $3 \times R_{200}$ of UDS-OD5 (left) and of UDS-OD6 (right). The red histograms show the redshift distribution of confirmed cluster members.

($M_* > 10^{10} M_\odot$). Not all of the red galaxies are quiescent. From the SED-fitting results, we find some of these red galaxies are dusty SF galaxies (shown as green squares in this figure). In this figure, blue hexagons are spectroscopically confirmed galaxies. As can be seen in the upper right panel of Figure 8, two red quiescent galaxies are spectroscopically confirmed as cluster members of the UDS-OD6 while the association of the other red sequence galaxies to the clusters is determined from photometric redshifts, the proximity to the overdense areas, and a statistical inference.

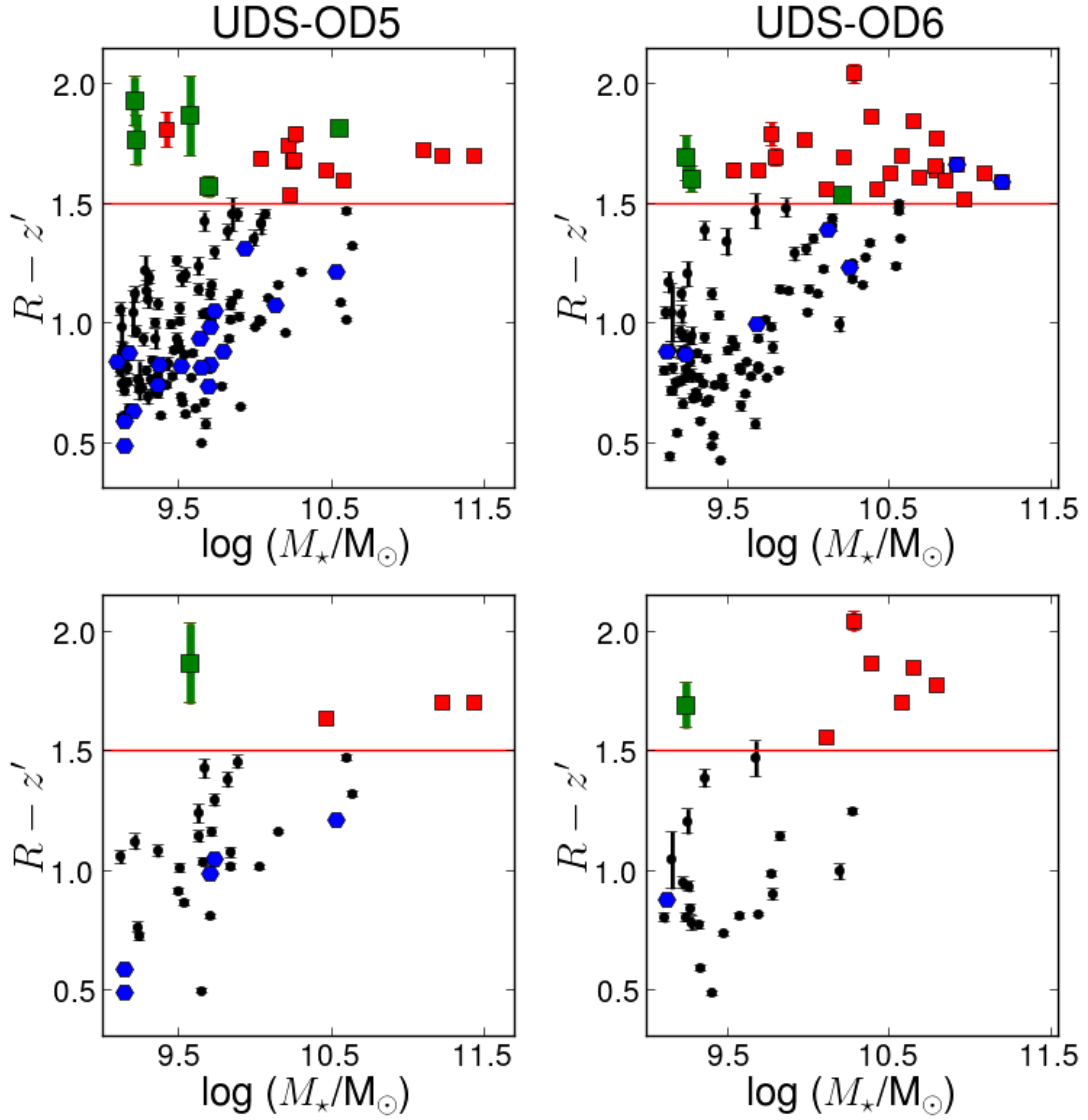


Figure 8. [Top panels]: Diagrams of $R-z'$ colors and stellar masses of galaxies within $3 \times R_{200}$ for UDS-OD5 (left) and UDS-OD6 (right). [Bottom panels]: Same diagrams for galaxies within R_{200} . Galaxies whose photometric (or spectroscopic if available) redshifts are within the range of the cluster are shown. Blue hexagons are spectroscopically confirmed galaxies and black small circles are galaxies with photometric redshift only. Red squares are red quiescent galaxies with $R-z'$ color greater than 1.5 and green squares are dusty star-forming galaxies with red color ($R-z' > 1.5$).

Table 3. Properties of confirmed clusters

Name	Redshift	σ_{gap}^a (km/s)	R_{200} (kpc)	$M_{200,v}^b$ (M_{\odot})	$M_{200,s}^c$ (M_{\odot})	QF_1^d	QF_2^e	FoF
(1)	(2)	(3)	(4)	(5)	(6)	(7)	(8)	(9)
UDS-OD5	0.954 ± 0.003	553 ± 87	799 ± 126	$1.70^{+0.94}_{-0.68} e+14$	$1.16^{+0.90}_{-0.51} e+14$	$0.18^{+0.11}_{-0.054}$	$0.094^{+0.11}_{-0.032}$	$0.056^{+0.013}_{-0.028}$
UDS-OD6	0.931 ± 0.003	518 ± 178	758 ± 261	$1.42^{+2.03}_{-1.02} e+14$	$1.27^{+0.99}_{-0.56} e+14$	$0.47^{+0.13}_{-0.12}$	$0.38^{+0.14}_{-0.11}$	$0.038^{+0.019}_{-0.0079}$

NOTE—(1) Cluster name; (2) Cluster redshift; (3) Velocity dispersion; (4) Cluster radius (R_{200}); (5) Cluster mass within $r \leq R_{200}$ derived from velocity dispersion; (6) Halo mass derived from total stellar mass using Lee et al. (2019) relation; (7) Quiescent Fraction calculated using method 1; (8) Quiescent Fraction calculated using method 2; (9) FoF fraction

^a Derived using gapper estimator (Beers et al. 1990)

^b Halo mass derived from σ_{gap} using Demarco et al. (2010) relation

^c Halo mass derived from total stellar mass using Lee et al. (2019) relation

^d Quiescent Fraction calculated using method 1

^e Quiescent Fraction calculated using method 2

3.3.2. Spatial distribution of galaxies of various types

Figure 9 shows the spatial distribution of various types of galaxies in and around UDS-OD5 (left panel) and UDS-OD6 (right panel), plotted over density maps. Here, the density map is drawn using galaxies whose (spectroscopic or photometric) redshifts are within the photometric redshift error range ($\Delta z / (1 + z_{cl}) = 0.028$).

In this figure, red circles show the locations of red (sequence) galaxies. We can see that there is a concentration of red (sequence) galaxies near the cluster center in the case of UDS-OD6. Black symbols are galaxies within the photometric redshift error range, and blue squares are spectroscopically confirmed galaxies among these. Purple stars are MIPS-detected galaxies which are dusty star-forming galaxies. Interestingly, near the cluster center of UDS-OD5

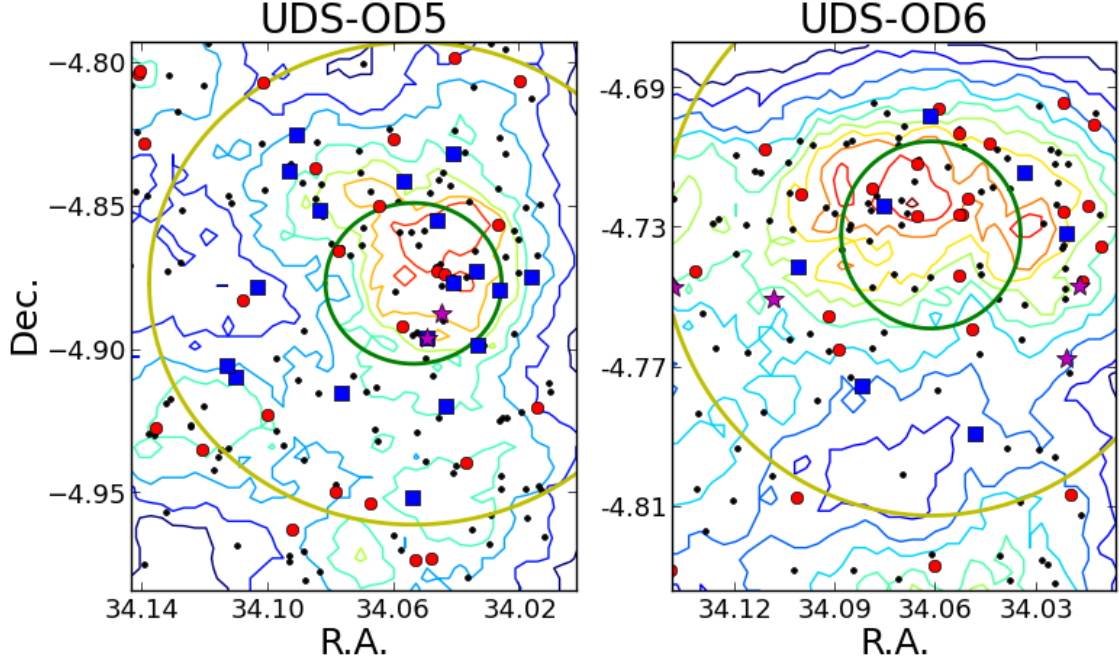


Figure 9. The location of various types of galaxies, plotted over the density maps of UDS-OD5 (left) and UDS-OD6 (right). Red circles show the locations of red (sequence) galaxies. Black dots show the location of galaxies whose photometric redshifts are within the photometric redshift error range ($\Delta z/(1+z_{cl}) = 0.028$) of each cluster and blue squares show spectroscopically confirmed galaxies. Purple stars show the MIPS-detected galaxies. The green and yellow circles in each panel show the R_{200} and $3 \times R_{200}$ of each cluster.

(left panel), there are concentration of various types of galaxies — red (sequence), SF, and dusty SF galaxies. while red (sequence) galaxies are more dominant in the central region of UDS-OD6 (right panel).

4. ANALYSIS

4.1. Correlation between the Quiescent Galaxy Fraction and the Large Scale Environment

In our previous work, we found that there is a correlation between the QF of high-redshift ($0.65 \leq z \leq 1.3$) galaxy clusters and the extent of large scale structure surrounding the clusters (Lee et al. 2019). Now, we investigate the QFs of the two newly confirmed clusters and large-scale overdensity surrounding them. For this analysis, we use both spectroscopic and photometric redshifts.

A galaxy is classified as quiescent if its specific SFR is smaller than $1/(3 \times t(z))$, where $t(z)$ is the age of the Universe at redshift z (Damen et al. 2009; Lee et al. 2015). Then, the quiescent galaxy fraction of a cluster is defined as the fraction of quiescent galaxies among total cluster member galaxies within R_{200} . In this work, we applied a stellar mass cut of $\log(M_*/M_\odot) \geq 9.1$, which is the stellar mass completeness limit, calculated in Lee et al. (2015).

We calculate the QF for each cluster in two ways. First, it is calculated by applying the weight (w) values which are derived as explained below (in a similar way as in Lee et al. 2019) to all galaxies within photometric redshift range ($\Delta z \leq 0.028 \times (1+z)$). The weight, w is computed as the number of spectroscopically confirmed cluster member galaxies divided by the sum of the number of spectroscopic members and outliers. For spectroscopically confirmed cluster members, we assign $w = 1$. The QF values calculated in this way (method 1) are $0.18_{-0.054}^{+0.11}$ for UDS-OD5 and $0.47_{-0.12}^{+0.13}$ for UDS-OD6.

Here, the errors are the 68.3% confidence levels, which have been determined employing the method outlined in Cameron (2011).

The second way (method 2) we used is to apply the background correction to the quiescent galaxy numbers of clusters by subtracting the quiescent galaxy fraction of field galaxies in the same redshift range to calculate the corrected quiescent galaxy number of each cluster, $N_{qs,cl,excess}$, as follows:

$$N_{qs,cl,excess} = N_{qs,cl,raw} - n_{qs,fld} \times A_{cl}, \quad (4)$$

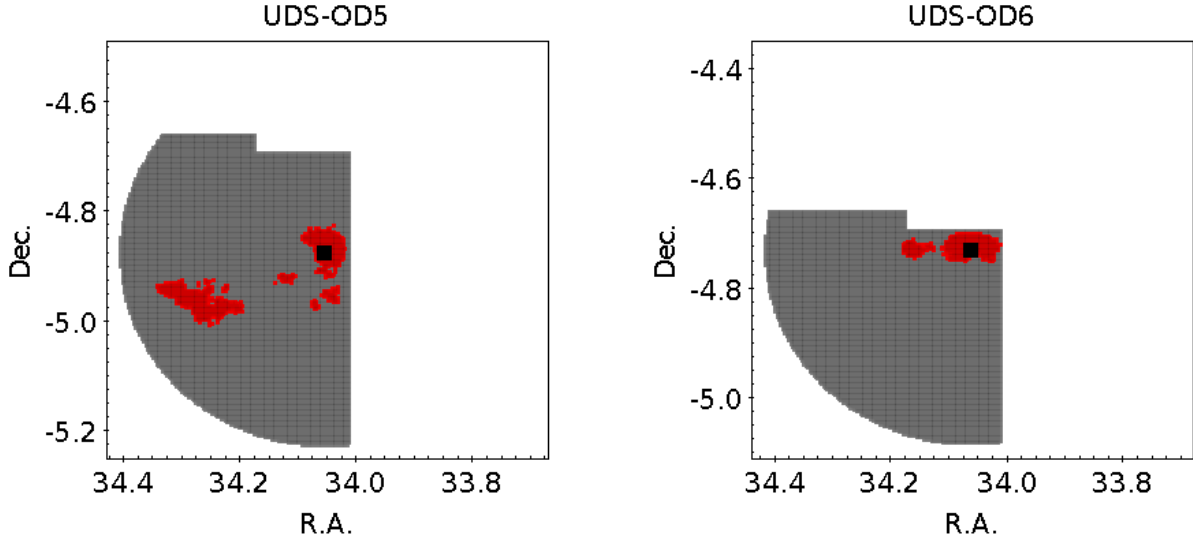


Figure 10. Distribution of the overdense ($\geq 2\sigma$) large-scale structure (shown as red regions) near UDS-OD5 (left) and UDS-OD6(right). The grey region shows the total area whose boundary is set by either 10 Mpc radius from the cluster center or by the survey boundary. The black square in each panel shows the location of the cluster center.

where $N_{qs,cl,raw}$ is the number of quiescent galaxies within R_{200} of the cluster, $n_{qs,fld}$ is the surface number density of quiescent galaxies in the field region, and A_{cl} is the surface area of the cluster. The quiescent galaxy fraction values calculated in this way (method 2) are $0.094^{+0.11}_{-0.032}$ and $0.38^{+0.14}_{-0.11}$ for UDS-OD5 and UDS-OD6, respectively.

In both methods, we use both the spectroscopically confirmed members and the candidate member galaxies with photometric redshift only. While we found and confirmed the cluster members out to $3 \times R_{200}$, we calculate the QF within R_{200} for consistent comparison with our previous work (Lee et al. 2015). The QF values tend to decrease when we use a larger radius, and this tendency was more significant for UDS-OD6. Both methods give higher QF for UDS-OD6.

As shown in the right panel of Figure 7, the spectroscopic redshift distribution of UDS-OD6 has several minor peaks in addition to the peak at the redshift of UDS-OD6. This might raise a question about the possible contamination of background galaxies belonging to minor peaks in calculating QF. However, our QF calculation methods can minimize this effect by applying a weight based on the spectroscopic redshifts (method 1), or by subtracting QF of field galaxies (method 2) minimizing the contamination effect in measuring QF. Also, the effect of possible remaining contamination from background galaxies, if any, would have made the QF underestimated (because the QF of field galaxies is lower than the QF of clusters), which strengthens our conclusion about the correlation between QF and FoF fraction.

To quantify the extent of large-scale structure surrounding the clusters, we use the friends-fo-friends fraction (FoF fraction) following Lee et al. (2019). The FoF fraction is defined as the fraction of (2-dimensional) overdense regions which are connected to a cluster over the total area within 10 Mpc radius around the cluster. Here, the overdense region is where the galaxy number density is greater than 2σ from the mean background number density. And, whether this overdense region is connected to the cluster is determined using FoF algorithm. So, if there are more overdense structures connected to the cluster, it has a larger FoF fraction. To calculate the FoF fraction, we use both photometric and spectroscopic redshifts. The results of FoF fraction measurement are shown in Figure 10. In this figure, the red-colored region shows the area where the connected overdense LSS and the black square symbol shows the location of each cluster center.

The FoF fractions of UDS-OD5 and UDS-OD6 are $0.056^{+0.013}_{-0.028}$ and $0.038^{+0.019}_{-0.0079}$, respectively. As can be seen in Figure 10, the FoF fractions cannot be measured within a full circle of 10 Mpc radius for both clusters, because these clusters are located near survey boundary. The uncertainty of FoF fraction is measured through Monte Carlo simulation. We assume the FoF fraction value in *unseen* region follows similar distribution as the FoF values found in our previous work (Lee et al. 2019, please refer Figure 11). Then we randomly pick FoF value of *unseen* region, assuming gaussian distribution and calculate the *total* FoF fraction combining this randomly picked value and the

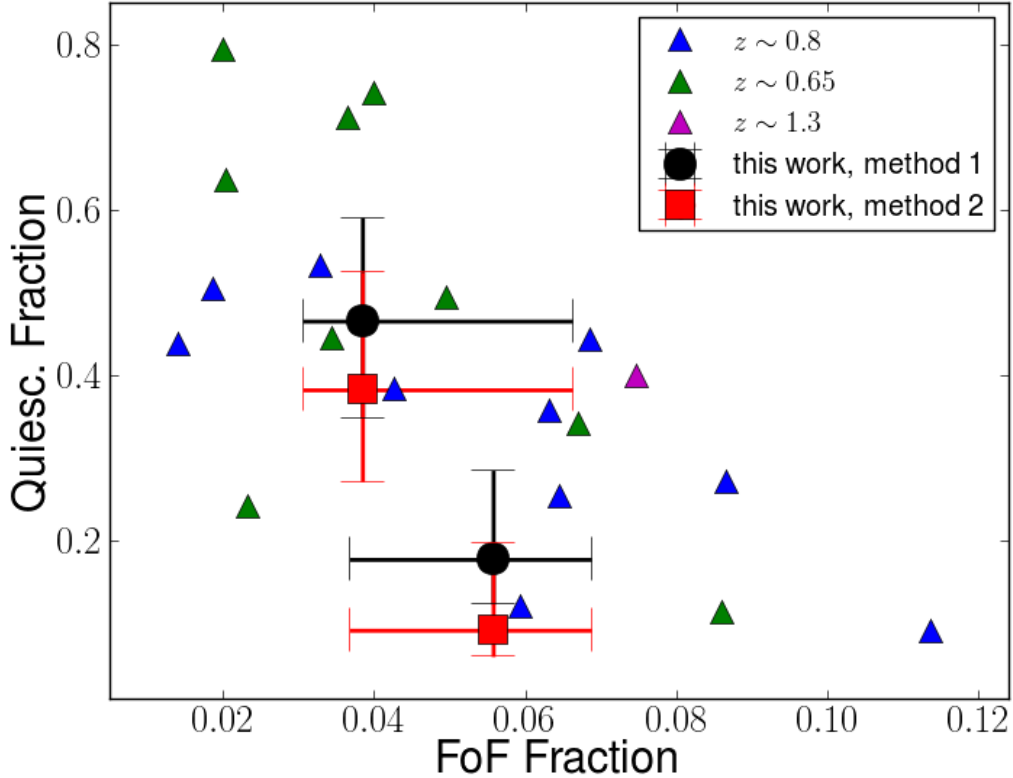


Figure 11. The correlation between quiescent galaxy fractions and FoF fractions of high redshift ($0.65 \leq z \leq 1.3$) galaxy clusters. Green, blue and purple triangles show the values of galaxy clusters at $z \sim 0.65$, 0.8 , and 1.3 , respectively from Lee et al. (2019). Black circles and red squares show the values of this study. The black circles and red squares show the QF values calculated following the methods 1 and 2, respectively (Please refer to the corresponding text for the explanation of each calculating method). Two clusters newly found in this study are consistent with the anti-correlation found in our previous work (Lee et al. 2019).

measured FoF fraction. We repeat this procedure 1000 times, and the uncertainty is determined as the 68% confidence interval.

These newly-found two clusters have different QFs, while being at similar redshifts and having similar masses. Their large scale environments as judged from the FoF fractions may be different but the two FoF values are within $1\text{-}\sigma$ errors. In Figure 11, we show the correlation between QFs and FoF fractions of these two clusters (black circles and red squares) along with the clusters from our previous work (Lee et al. 2019). In this figure, we can see that these newly-found two clusters do not behave differently from the anti-correlation between QF and FoF fraction found in Lee et al. (2019).

4.2. Cluster Stellar Mass Function

Now, we investigate the stellar mass function of confirmed clusters. Figure 12 shows the stellar mass functions of quiescent (red histograms) and star-forming galaxies (blue histograms) which are within R_{200} of UDS-OD5 (left panels) and of UDS-OD6 (right panels). In calculating these stellar mass functions of cluster galaxies, we apply appropriate weights (see Section 4.1) to galaxies with only photometric redshifts.

As can be seen in this figure, the stellar mass functions of quiescent galaxies in UDS-OD5 and UDS-OD6 are very similar (bottom panels). However, the stellar mass functions of star-forming galaxies of these two clusters are largely different (top panels). The stellar mass function of star-forming galaxies of UDS-OD5 shows a clear excess compared to that of UDS-OD6. This excess of star-forming galaxies of UDS-OD5 leads to a lower QF than UDS-OD6. Considering the fact that there are more overdense structures surrounding UDS-OD5 than UDS-OD6, we can speculate that these

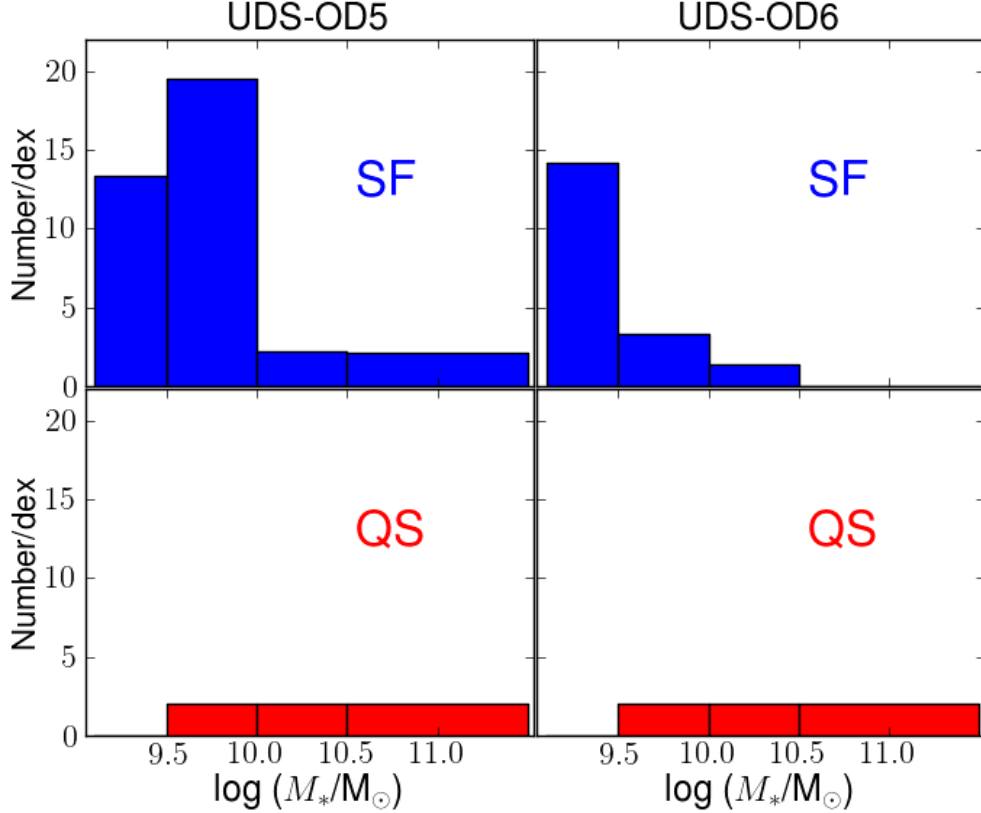


Figure 12. The stellar mass functions of star-forming (top panels) and quiescent (bottom panels) galaxies of UDS-OD5 (left panels) and UDS-OD6 (right panels). Candidate cluster members without spectroscopic confirmation are included with appropriate weights applied.

additional star-forming galaxies have accreted from the surrounding overdense structure, in good accordance with our suggested WFM.

Galaxies become quiescent through two distinct mechanisms: in-situ and accretion. The in-situ process suggests that the evolution of quiescent galaxies is dependent on their mass, with more massive galaxies transitioning to the red sequence at higher redshifts (Sánchez-Blázquez et al. 2009). The formation of quiescent galaxies, whether through in-situ processes or accretion, exhibits distinct dependencies on redshift and environment. In the early universe, in-situ star formation prevails, causing galaxies to transition from active star formation to quiescence over time. Massive galaxies become quenched and red as early as $z > 2$ (Kriek et al. 2008; Gabor & Davé 2012). On the other hand, accretion becomes more significant in the late-time universe, with a potential increase in its contribution over cosmic time, especially for low-mass galaxies (Peng et al. 2015; Lee et al. 2015; Cerulo et al. 2016). Dense environments and large-scale structures, such as galaxy clusters, play crucial roles in facilitating accretion processes.

In Figure 12, it is evident there is no difference in the stellar-mass functions of quiescent galaxies between the two clusters. Additionally, it is noteworthy that there are no quiescent galaxies with $\log M_*/M_\odot < 9.5$ in either cluster, suggesting that the environmental factors may not be fully at play yet. In case of the stellar mass functions of SF galaxies, we observe a higher presence of low-mass SF galaxies in OD5. We hypothesize that these galaxies, relatively recently accreted from the surrounding large-scale structure, will cease star formation over time due to environmental factors and eventually join the red sequence. Consequently, over time, OD5 is expected to harbor a larger number of red sequence galaxies compared to OD6.

Figure 13 shows the stellar-mass dependent QFs of UDS-OD5 (blue histograms) and UDS-OD6 (red histograms), within R_{200} of each cluster. In both clusters, we can see a clear stellar-mass dependence of cluster QF, in a sense that QF is higher for more massive galaxies. Also, we can see that quiescent galaxy fractions of UDS-OD5 are lower than UDS-OD6 in three (out of four) mass bins, which leads to the lower total quiescent galaxy fraction of UDS-

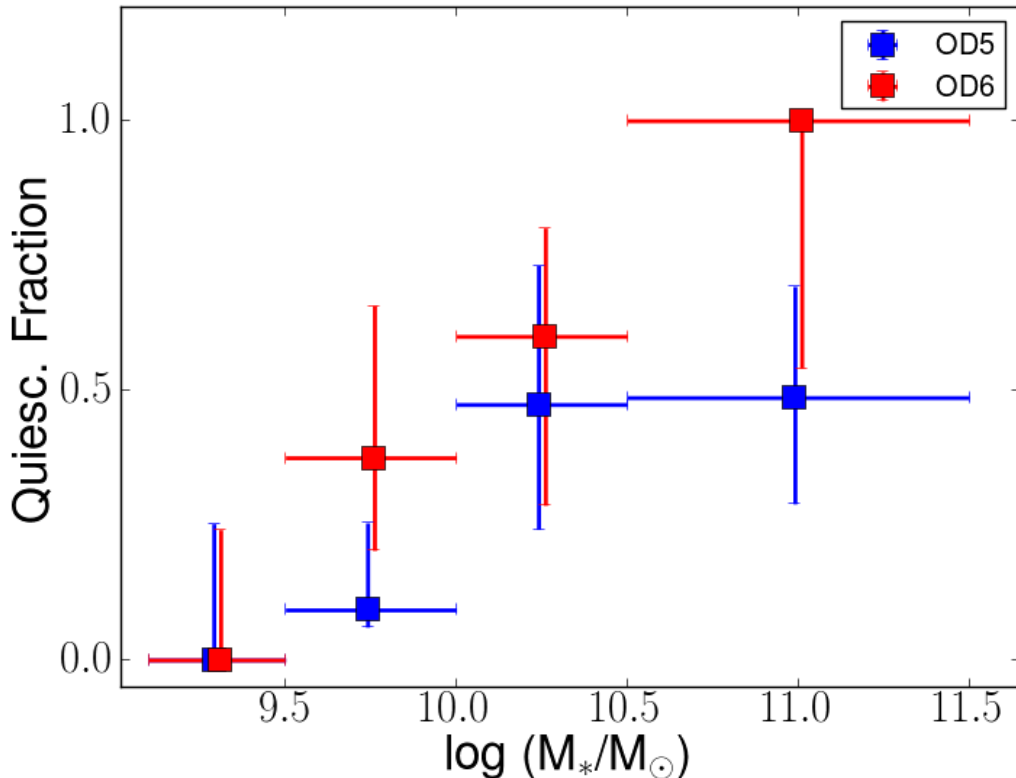


Figure 13. The stellar-mass dependent quiescent galaxy fraction within R_{200} of UDS-OD5 (blue squares) and of UDS-OD6 (red squares). Candidate cluster members without spectroscopic confirmation are included with appropriate weights applied. As can be seen here, OD6 has larger QFs in three stellar mass bins.

OD5. As mentioned above, this difference is speculated to be originated by recently fallen galaxies from surrounding environment.

Stellar-mass dependent trend in QFs shown in Figure 13 indicates that QF would increase if we apply a higher stellar-mass cut for both UDS-OD5 and UDS-OD6. But, the change of stellar-mass cut would not change our main conclusion, since this stellar-mass dependent trend is shown in both clusters in a similar manner.

5. CONCLUSION

We conducted spectroscopic observations of galaxies with a redshift of $z \sim 0.95$ in and around galaxy cluster candidates identified in the UDS field using Magellan/IMACS. We present the flux-calibrated spectra and redshifts of 105 galaxies for which redshift measurements were possible. Through the analysis of these 105 spectroscopic redshifts, we have identified two galaxy clusters: one at $z \sim 0.95$ (UDS-OD5) and another at $z \sim 0.93$ (UDS-OD6). Additionally, by integrating spectroscopic redshift information with multi-band photometric data, we have made the following findings:

1. The identified clusters exhibit halo masses of $M_{200} \sim 10^{14} M_\odot$, and sizes of $R_{200} \sim 0.8$ Mpc. Specifically, for UDS-OD5, the estimated halo mass is $M_{200} = 1.7 \times 10^{14} M_\odot$ with a corresponding size of $R_{200} = 800$ kpc, derived from spectroscopic redshift information. Similarly, for UDS-OD6, the values are $M_{200} = 1.4 \times 10^{14} M_\odot$ and $R_{200} = 760$ kpc. We have also estimated the halo masses using the correlation between total stellar mass and halo mass presented in Lee et al. (2019). This method yields halo mass estimates of $M_{200} = 1.2 \times 10^{14} M_\odot$ for UDS-OD5 and $1.3 \times 10^{14} M_\odot$ for UDS-OD6, which are consistent with the values derived from spectroscopic redshifts.

2. Despite their similar masses, sizes, and redshifts, these two clusters exhibit distinct star formation properties. While a well-formed red sequence exists, UDS-OD5 shows a prevalence of blue, star-forming galaxies. The quiescent galaxy fraction for UDS-OD5 is estimated to be 0.18 ± 0.097 (method 1) or 0.094 ± 0.071 (method 2). In contrast, UDS-OD6 displays a higher quiescent fraction of 0.47 ± 0.21 (method 1) or 0.38 ± 0.20 (method 2) with many red sequence galaxies, particularly concentrated in the cluster’s central region.
3. While the limited coverage of the surrounding area introduces some uncertainty, it appears that these two clusters inhabit different large-scale environments. The FoF fraction values for UDS-OD5 and UDS-OD6 are $0.056^{+0.013}_{-0.028}$ and $0.038^{+0.019}_{-0.0079}$, respectively. These FoF values and QF values of these two clusters are consistent with the (anti-)correlation observed in high-redshift ($0.65 \leq z \leq 1.3$) clusters as reported in Lee et al. (2019), supporting our suggested WFM.
4. We examine the stellar mass function of cluster galaxies for distinct populations of quiescent and star-forming galaxies. Both UDS-OD5 and UDS-OD6 show similar quiescent galaxy stellar mass functions. However, there is a discrepancy in the stellar mass functions of star-forming galaxies between the two clusters. UDS-OD5 displays an overabundance of star-forming galaxies compared to UDS-OD6. We propose that this excess of star-forming galaxies found in UDS-OD5 stems from recent infall of galaxies from the surrounding large-scale environment, providing further support for our WFM.

Our spectroscopic data will be valuable for future studies of galaxies in the UDS field. The properties of the two newly confirmed clusters at $z \sim 0.95$ are consistent with our previously suggested WFM. Future studies on this correlation over a larger area and employing more extensive multi-object spectroscopy would provide a deeper understanding about the interplay between galaxy clusters and LSS, as well as its impact on the evolution of galaxy clusters.

This work was supported by the National Research Foundation of Korea (NRF) grant No. 2020R111A1A01060310, No. 2020R1A2C3011091 and No. 2021M3F7A1084525, funded by the Korea government (MSIT). This paper includes data gathered with the 6.5 m Magellan Telescopes located at Las Campanas Observatory, Chile, and from the UKIDSS (Lawrence et al. 2007) UDS (Almaini et al. 2007) project. UKIDSS uses the UKIRT Wide Field Camera (WFCAM; Casali et al. 2007). The photometric system is described in Hewett et al. (2006), and the calibration is described in Hodgkin et al. (2009). The pipeline processing and science archive are described in Hambly et al. (2008).

Facilities: Magellan(IMACS), UKIRT(WFCAM), Subaru(SUPRIMECAM), Spitzer(IRAC)

APPENDIX

A. FLUX CALIBRATED GALAXY SPECTRA

We reduced the Magellan MOS spectra using the COSMOS2 software. This reduction process encompassed several key steps, namely wavelength calibration, flat fielding, bias subtraction, and sky subtraction. This process resulted in a set of processed 2D spectra, which were then combined to generate 1D spectra.

For these resulting 1D spectra, we conducted flux calibration by referencing a star’s spectrum specifically included in the Magellan mask for calibration purposes. This calibration was established by comparing the Magellan spectrum of the star with its counterpart from the Sloan Digital Sky Survey (SDSS).

We provide the flux calibrated spectra of all the galaxies from Table 1 in a machine-readable form (Table A1). We also show spectra of galaxies from Table 1 in Figure A1.

REFERENCES

- | | |
|---|---|
| Abadi, M. G., Moore, B., & Bower, R. G. 1999, MNRAS, 308, 947, doi: 10.1046/j.1365-8711.1999.02715.x | Alberts, S., Pope, A., Brodwin, M., et al. 2016, ApJ, 825, 72, doi: 10.3847/0004-637X/825/1/72 |
|---|---|

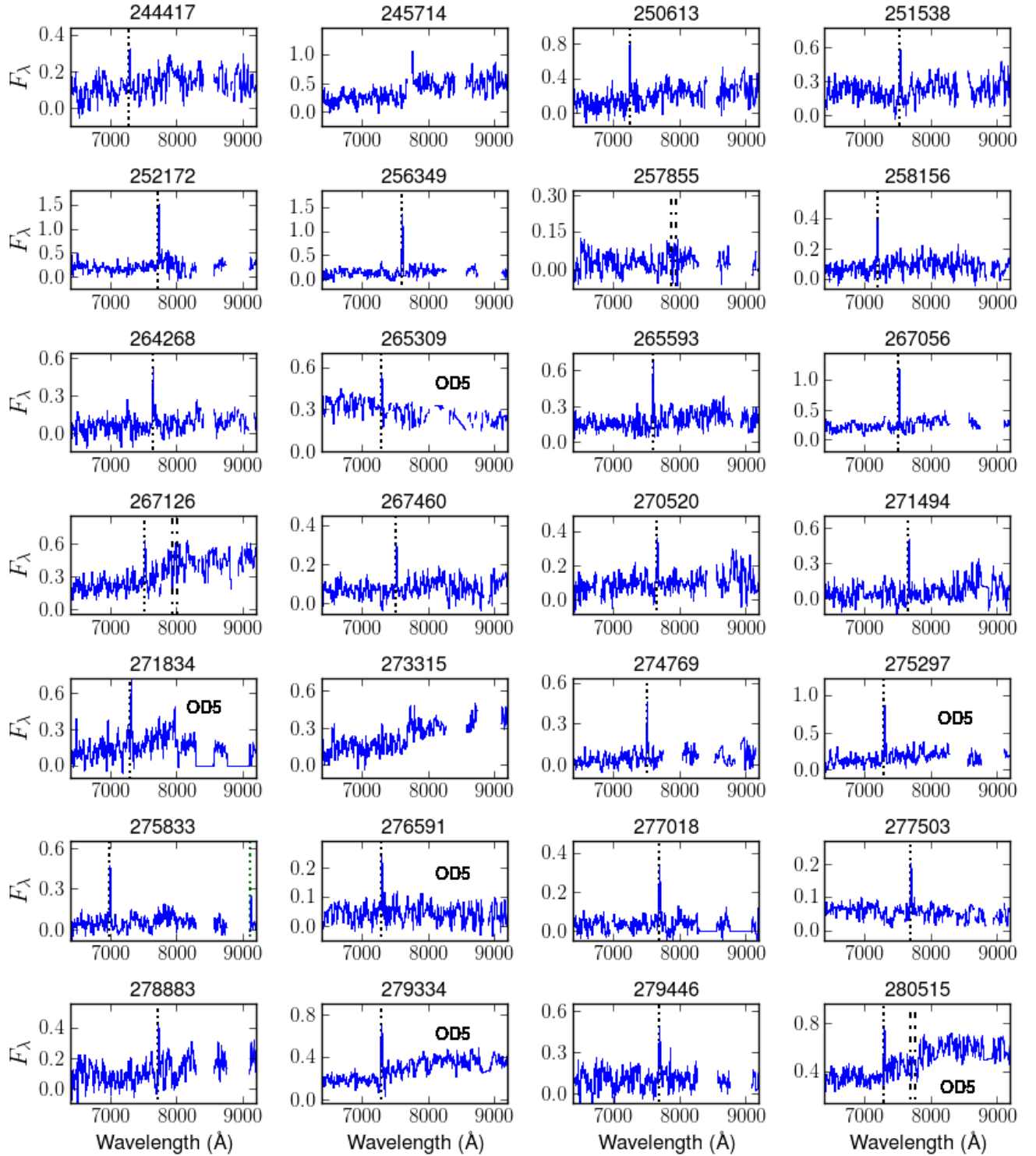


Figure A1. Spectra of spectroscopically confirmed from Table 1. The y -axis is in the unit of $10^{-17} \text{ erg s}^{-1} \text{ cm}^{-2} \text{ \AA}^{-1}$. The colored dotted lines show the locations of various emission lines as follows: black-[O II], green-H β , red-H δ , orange-[O III], magenta-H γ . The black dot-dashed lines show the location of redshifted Ca H&K absorption lines.

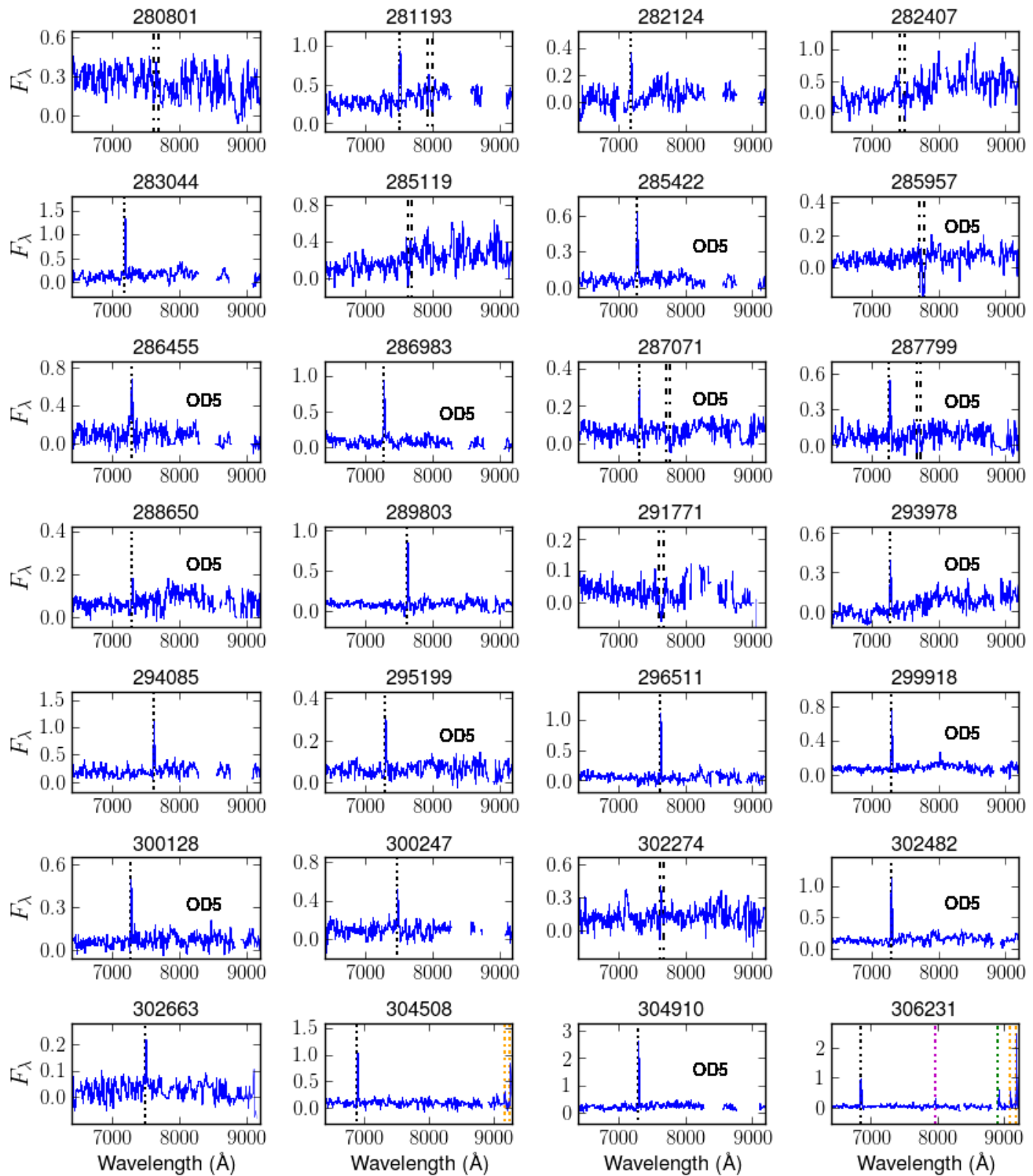


Figure A1. continued

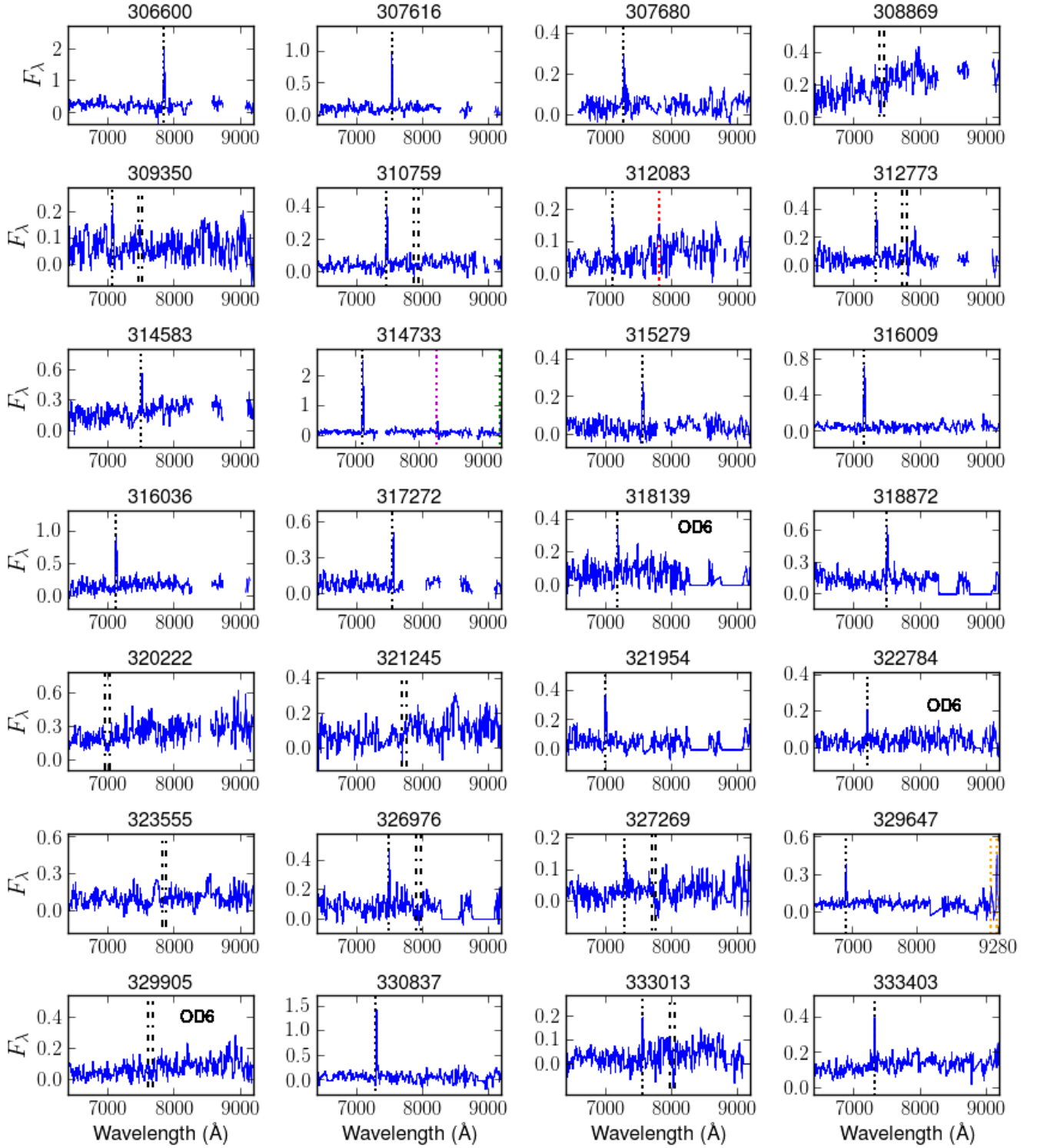


Figure A1. continued

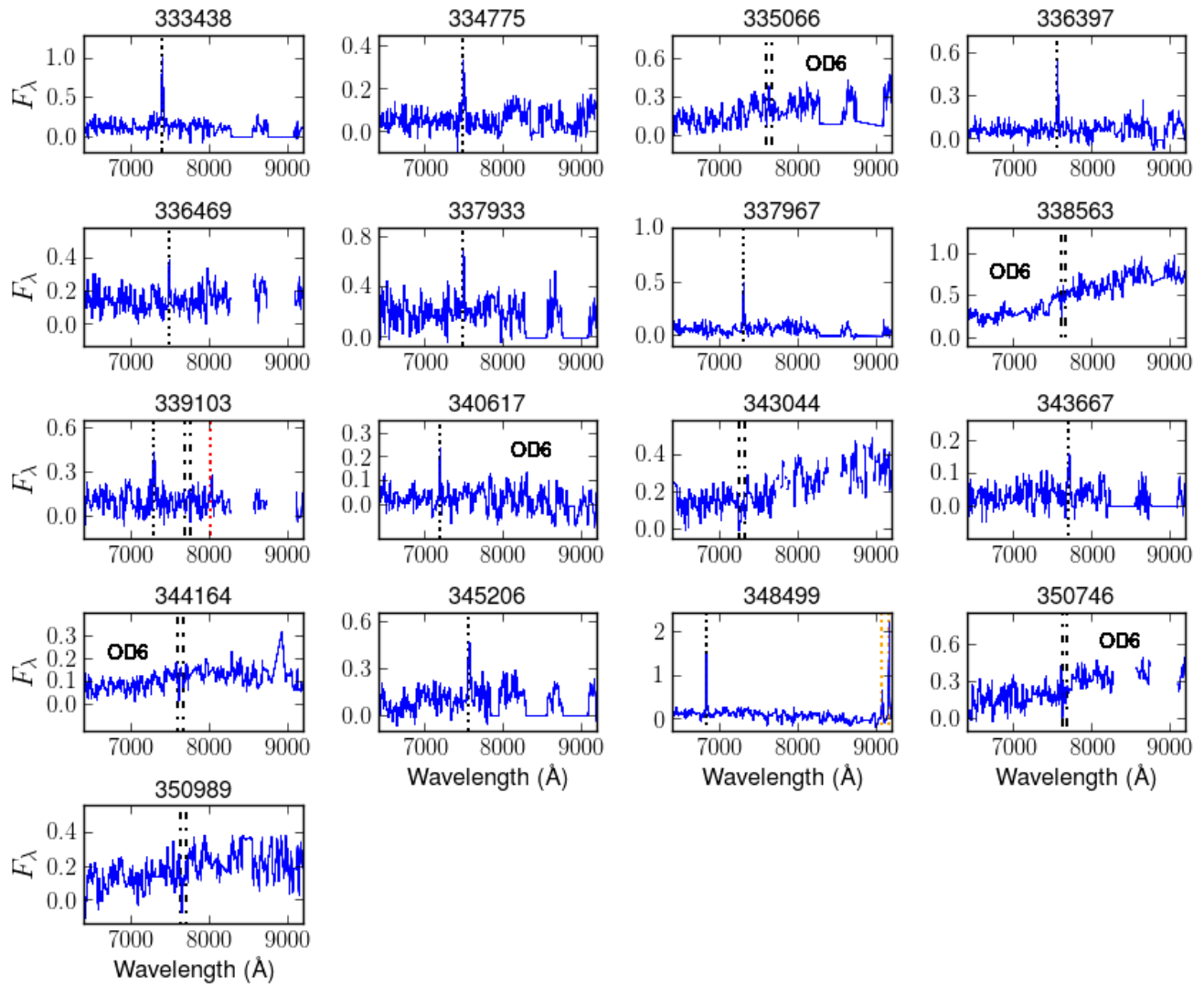


Figure A1. continued

Table A1. Flux-calibrated spectrum of the galaxy with ID number 314733. (Abbreviated. Full spectra of all galaxies are provided in FITS format.)

Wavelength (\AA)	Flux ($10^{-17} \text{ erg s}^{-1} \text{ cm}^{-2} \text{\AA}^{-1}$)	Flux Error ($10^{-17} \text{ erg s}^{-1} \text{ cm}^{-2} \text{\AA}^{-1}$)
5698.0	0.0000	1.6128E-4
5700.0	0.0992	1.6016E-4
5702.0	0.1067	1.6468E-4
5704.0	0.0312	1.7731E-4
5706.0	0.1007	1.6318E-4
5708.0	0.0940	1.5242E-4
5710.0	0.2542	1.4999E-4
5712.0	0.2646	1.5910E-4
5714.0	0.2750	1.6044E-4
5716.0	0.2043	1.6650E-4
5718.0	0.0931	1.7095E-4
5720.0	0.0878	1.5808E-4
5722.0	0.0894	1.6296E-4
5724.0	0.1374	1.7439E-4
5726.0	0.1259	1.5464E-4
5728.0	0.1290	1.5850E-4
5730.0	0.1334	1.5312E-4
.....

NOTE—Table A1 is published in its entirety in the machine-readable format. A portion is shown here for guidance regarding its form and content.

- Almaini, O., Foucaud, S., Lane, K., et al. 2007, in *Astronomical Society of the Pacific Conference Series*, Vol. 379, *Cosmic Frontiers*, ed. N. Metcalfe & T. Shanks, 163
- Baldry, I. K., Balogh, M. L., Bower, R. G., et al. 2006, *MNRAS*, 373, 469, doi: [10.1111/j.1365-2966.2006.11081.x](https://doi.org/10.1111/j.1365-2966.2006.11081.x)
- Balogh, M. L., Navarro, J. F., & Morris, S. L. 2000, *ApJ*, 540, 113, doi: [10.1086/309323](https://doi.org/10.1086/309323)
- Beers, T. C., Flynn, K., & Gebhardt, K. 1990, *AJ*, 100, 32, doi: [10.1086/115487](https://doi.org/10.1086/115487)
- Brammer, G. B., van Dokkum, P. G., & Coppi, P. 2008, *ApJ*, 686, 1503, doi: [10.1086/591786](https://doi.org/10.1086/591786)
- Bruzual, G., & Charlot, S. 2003, *MNRAS*, 344, 1000, doi: [10.1046/j.1365-8711.2003.06897.x](https://doi.org/10.1046/j.1365-8711.2003.06897.x)
- Calzetti, D., Armus, L., Bohlin, R. C., et al. 2000, *ApJ*, 533, 682, doi: [10.1086/308692](https://doi.org/10.1086/308692)
- Cameron, E. 2011, *PASA*, 28, 128, doi: [10.1071/AS10046](https://doi.org/10.1071/AS10046)
- Caputi, K. I., Dole, H., Lagache, G., et al. 2006, *ApJ*, 637, 727, doi: [10.1086/498497](https://doi.org/10.1086/498497)
- Casali, M., Adamson, A., Alves de Oliveira, C., et al. 2007, *A&A*, 467, 777, doi: [10.1051/0004-6361:20066514](https://doi.org/10.1051/0004-6361:20066514)
- Cerulo, P., Couch, W. J., Lidman, C., et al. 2016, *MNRAS*, 457, 2209, doi: [10.1093/mnras/stw080](https://doi.org/10.1093/mnras/stw080)
- Chabrier, G. 2003, *PASP*, 115, 763, doi: [10.1086/376392](https://doi.org/10.1086/376392)
- Chartab, N., Mobasher, B., Darvish, B., et al. 2020, *ApJ*, 890, 7, doi: [10.3847/1538-4357/ab61fd](https://doi.org/10.3847/1538-4357/ab61fd)
- Clemens, M. S., Bressan, A., Nikolic, B., et al. 2006, *MNRAS*, 370, 702, doi: [10.1111/j.1365-2966.2006.10530.x](https://doi.org/10.1111/j.1365-2966.2006.10530.x)
- Damen, M., Labbé, I., Franx, M., et al. 2009, *ApJ*, 690, 937, doi: [10.1088/0004-637X/690/1/937](https://doi.org/10.1088/0004-637X/690/1/937)
- Demarco, R., Wilson, G., Muzzin, A., et al. 2010, *ApJ*, 711, 1185, doi: [10.1088/0004-637X/711/2/1185](https://doi.org/10.1088/0004-637X/711/2/1185)
- Ellingson, E., Lin, H., Yee, H. K. C., & Carlberg, R. G. 2001, *ApJ*, 547, 609, doi: [10.1086/318423](https://doi.org/10.1086/318423)
- Fitzpatrick, P. J., & Graves, G. J. 2015, *MNRAS*, 447, 1383, doi: [10.1093/mnras/stu2509](https://doi.org/10.1093/mnras/stu2509)
- Furusawa, H., Kosugi, G., Akiyama, M., et al. 2008, *ApJS*, 176, 1, doi: [10.1086/527321](https://doi.org/10.1086/527321)
- Gabor, J. M., & Davé, R. 2012, *MNRAS*, 427, 1816, doi: [10.1111/j.1365-2966.2012.21640.x](https://doi.org/10.1111/j.1365-2966.2012.21640.x)
- Gu, Y., Fang, G., Yuan, Q., Lu, S., & Liu, S. 2021, *ApJ*, 921, 60, doi: [10.3847/1538-4357/ac1ce0](https://doi.org/10.3847/1538-4357/ac1ce0)
- Gunn, J. E., & Gott, J. Richard, I. 1972, *ApJ*, 176, 1, doi: [10.1086/151605](https://doi.org/10.1086/151605)
- Hambly, N. C., Collins, R. S., Cross, N. J. G., et al. 2008, *MNRAS*, 384, 637, doi: [10.1111/j.1365-2966.2007.12700.x](https://doi.org/10.1111/j.1365-2966.2007.12700.x)

- Hartwick, F. D. A. 2004, *ApJ*, 603, 108, doi: [10.1086/381425](https://doi.org/10.1086/381425)
- Hayashi, M., Koyama, Y., Kodama, T., et al. 2019, *PASJ*, 71, 112, doi: [10.1093/pasj/psz097](https://doi.org/10.1093/pasj/psz097)
- Heavens, A., Panter, B., Jimenez, R., & Dunlop, J. 2004, *Nature*, 428, 625, doi: [10.1038/nature02474](https://doi.org/10.1038/nature02474)
- Henriques, B. M. B., White, S. D. M., Thomas, P. A., et al. 2015, *MNRAS*, 451, 2663, doi: [10.1093/mnras/stv705](https://doi.org/10.1093/mnras/stv705)
- Hewett, P. C., Warren, S. J., Leggett, S. K., & Hodgkin, S. T. 2006, *MNRAS*, 367, 454, doi: [10.1111/j.1365-2966.2005.09969.x](https://doi.org/10.1111/j.1365-2966.2005.09969.x)
- Hodgkin, S. T., Irwin, M. J., Hewett, P. C., & Warren, S. J. 2009, *MNRAS*, 394, 675, doi: [10.1111/j.1365-2966.2008.14387.x](https://doi.org/10.1111/j.1365-2966.2008.14387.x)
- Im, M., Griffiths, R. E., & Ratnatunga, K. U. 1997, *ApJ*, 475, 457, doi: [10.1086/303583](https://doi.org/10.1086/303583)
- Jimenez, R., Panter, B., Heavens, A. F., & Verde, L. 2005, *MNRAS*, 356, 495, doi: [10.1111/j.1365-2966.2004.08469.x](https://doi.org/10.1111/j.1365-2966.2004.08469.x)
- Kauffmann, G., White, S. D. M., Heckman, T. M., et al. 2004, *MNRAS*, 353, 713, doi: [10.1111/j.1365-2966.2004.08117.x](https://doi.org/10.1111/j.1365-2966.2004.08117.x)
- Kauffmann, G., Heckman, T. M., White, S. D. M., et al. 2003, *MNRAS*, 341, 54, doi: [10.1046/j.1365-8711.2003.06292.x](https://doi.org/10.1046/j.1365-8711.2003.06292.x)
- Kennicutt, Robert C., J. 1998, *ARA&A*, 36, 189, doi: [10.1146/annurev.astro.36.1.189](https://doi.org/10.1146/annurev.astro.36.1.189)
- Knebe, A., Pearce, F. R., Thomas, P. A., et al. 2015, *MNRAS*, 451, 4029, doi: [10.1093/mnras/stv1149](https://doi.org/10.1093/mnras/stv1149)
- Kriek, M., van der Wel, A., van Dokkum, P. G., Franx, M., & Illingworth, G. D. 2008, *ApJ*, 682, 896, doi: [10.1086/589677](https://doi.org/10.1086/589677)
- Larson, R. B., Tinsley, B. M., & Caldwell, C. N. 1980, *ApJ*, 237, 692, doi: [10.1086/157917](https://doi.org/10.1086/157917)
- Lawrence, A., Warren, S. J., Almaini, O., et al. 2007, *MNRAS*, 379, 1599, doi: [10.1111/j.1365-2966.2007.12040.x](https://doi.org/10.1111/j.1365-2966.2007.12040.x)
- Lee, S.-K., Ferguson, H. C., Somerville, R. S., et al. 2014, *ApJ*, 783, 81, doi: [10.1088/0004-637X/783/2/81](https://doi.org/10.1088/0004-637X/783/2/81)
- Lee, S.-K., Ferguson, H. C., Somerville, R. S., Wiklind, T., & Giavalisco, M. 2010, *ApJ*, 725, 1644, doi: [10.1088/0004-637X/725/2/1644](https://doi.org/10.1088/0004-637X/725/2/1644)
- Lee, S.-K., Idzi, R., Ferguson, H. C., et al. 2009, *ApJS*, 184, 100, doi: [10.1088/0067-0049/184/1/100](https://doi.org/10.1088/0067-0049/184/1/100)
- Lee, S.-K., Im, M., Hyun, M., et al. 2019, *MNRAS*, 490, 135, doi: [10.1093/mnras/stz2564](https://doi.org/10.1093/mnras/stz2564)
- Lee, S.-K., Im, M., Kim, J.-W., et al. 2015, *ApJ*, 810, 90, doi: [10.1088/0004-637X/810/2/90](https://doi.org/10.1088/0004-637X/810/2/90)
- Lemaux, B. C., Tomczak, A. R., Lubin, L. M., et al. 2019, *MNRAS*, 490, 1231, doi: [10.1093/mnras/stz2661](https://doi.org/10.1093/mnras/stz2661)
- Lewis, I., Balogh, M., De Propriis, R., et al. 2002, *MNRAS*, 334, 673, doi: [10.1046/j.1365-8711.2002.05558.x](https://doi.org/10.1046/j.1365-8711.2002.05558.x)
- Longhetti, M., Bressan, A., Chiosi, C., & Rampazzo, R. 1999, *A&A*, 345, 419, doi: [10.48550/arXiv.astro-ph/9903315](https://doi.org/10.48550/arXiv.astro-ph/9903315)
- Lu, S., Fang, G., Gu, Y., et al. 2021, *ApJ*, 913, 81, doi: [10.3847/1538-4357/abf4d7](https://doi.org/10.3847/1538-4357/abf4d7)
- Lubin, L. M., Gal, R. R., Lemaux, B. C., Kocevski, D. D., & Squires, G. K. 2009, *AJ*, 137, 4867, doi: [10.1088/0004-6256/137/6/4867](https://doi.org/10.1088/0004-6256/137/6/4867)
- Madau, P. 1995, *ApJ*, 441, 18, doi: [10.1086/175332](https://doi.org/10.1086/175332)
- Madau, P., & Dickinson, M. 2014, *ARA&A*, 52, 415, doi: [10.1146/annurev-astro-081811-125615](https://doi.org/10.1146/annurev-astro-081811-125615)
- Madau, P., Ferguson, H. C., Dickinson, M. E., et al. 1996, *MNRAS*, 283, 1388, doi: [10.1093/mnras/283.4.1388](https://doi.org/10.1093/mnras/283.4.1388)
- Masters, D., & Capak, P. 2011, *PASP*, 123, 638, doi: [10.1086/660023](https://doi.org/10.1086/660023)
- McNab, K., Balogh, M. L., van der Burg, R. F. J., et al. 2021, arXiv e-prints, arXiv:2109.03105, <https://arxiv.org/abs/2109.03105>
- Moore, B., Katz, N., Lake, G., Dressler, A., & Oemler, A. 1996, *Nature*, 379, 613, doi: [10.1038/379613a0](https://doi.org/10.1038/379613a0)
- Oemler, A., Clardy, K., Kelson, D., Walth, G., & Villanueva, E. 2017, COSMOS: Carnegie Observatories System for MultiObject Spectroscopy, Astrophysics Source Code Library, record ascl:1705.001, <http://ascl.net/1705.001>
- Oke, J. B. 1974, *ApJS*, 27, 21, doi: [10.1086/190287](https://doi.org/10.1086/190287)
- Pacifici, C., Kassin, S. A., Weiner, B., Charlot, S., & Gardner, J. P. 2013, *ApJL*, 762, L15, doi: [10.1088/2041-8205/762/1/L15](https://doi.org/10.1088/2041-8205/762/1/L15)
- Papovich, C., Kawinwanichakij, L., Quadri, R. F., et al. 2018, *ApJ*, 854, 30, doi: [10.3847/1538-4357/aaa766](https://doi.org/10.3847/1538-4357/aaa766)
- Peng, Y., Maiolino, R., & Cochrane, R. 2015, *Nature*, 521, 192, doi: [10.1038/nature14439](https://doi.org/10.1038/nature14439)
- Peng, Y.-j., Lilly, S. J., Kovač, K., et al. 2010, *ApJ*, 721, 193, doi: [10.1088/0004-637X/721/1/193](https://doi.org/10.1088/0004-637X/721/1/193)
- Quadri, R. F., Williams, R. J., Franx, M., & Hildebrandt, H. 2012, *ApJ*, 744, 88, doi: [10.1088/0004-637X/744/2/88](https://doi.org/10.1088/0004-637X/744/2/88)
- Renzini, A. 2009, *MNRAS*, 398, L58, doi: [10.1111/j.1745-3933.2009.00710.x](https://doi.org/10.1111/j.1745-3933.2009.00710.x)
- Sánchez-Blázquez, P., Jablonka, P., Noll, S., et al. 2009, *A&A*, 499, 47, doi: [10.1051/0004-6361/200811355](https://doi.org/10.1051/0004-6361/200811355)
- Sarron, F., & Conselice, C. J. 2021, *MNRAS*, 506, 2136, doi: [10.1093/mnras/stab1844](https://doi.org/10.1093/mnras/stab1844)
- Scoville, N., Arnouts, S., Aussel, H., et al. 2013, *ApJS*, 206, 3, doi: [10.1088/0067-0049/206/1/3](https://doi.org/10.1088/0067-0049/206/1/3)
- Sobral, D., Best, P. N., Smail, I., et al. 2011, *MNRAS*, 411, 675, doi: [10.1111/j.1365-2966.2010.17707.x](https://doi.org/10.1111/j.1365-2966.2010.17707.x)
- Somerville, R. S., & Davé, R. 2015, *ARA&A*, 53, 51, doi: [10.1146/annurev-astro-082812-140951](https://doi.org/10.1146/annurev-astro-082812-140951)

Tran, K.-V. H., van Dokkum, P., Illingworth, G. D., et al.
2005, ApJ, 619, 134, doi: [10.1086/426427](https://doi.org/10.1086/426427)

Vogelsberger, M., Marinacci, F., Torrey, P., & Puchwein, E.
2020, Nature Reviews Physics, 2, 42,
doi: [10.1038/s42254-019-0127-2](https://doi.org/10.1038/s42254-019-0127-2)